

Identifying resonances of the Galactic bar in *Gaia* DR2:

I. Clues from action space

Wilma H. Trick^{1*}, Francesca Fragkoudi¹, Jason A. S. Hunt^{2,3}, J. Ted Mackereth⁴,
and Simon D. M. White¹

¹Max-Planck-Institut für Astrophysik, Karl-Schwarzschild-Str. 1, D-85748 Garching b. München, Germany

²Dunlap Institute for Astronomy and Astrophysics, University of Toronto, 50 St. George Street, Toronto, Ontario, M5S 3H4, Canada

³Center for Computational Astrophysics, Flatiron Institute, 162 5th Av., New York City, NY 10010, USA

⁴School of Astronomy and Astrophysics, University of Birmingham, Edgbaston, Birmingham, B15 2TT, UK

Accepted XXX. Received YYY; in original form ZZZ

ABSTRACT

Action space synthesizes the orbital information of stars and is well-suited to analyse the rich kinematic substructure of the disc in the *Gaia* DR2 radial velocity sample (RVS). We revisit the strong perturbation induced in the Milky Way (MW) disc by an $m = 2$ bar, using test particle simulations and the actions (J_R, L_z, J_z) estimated in an axisymmetric potential. These make three useful diagnostics cleanly visible. (1.) We use the well-known characteristic flip from outward to inward motion at the Outer Lindblad Resonance (OLR, $l = +1, m = 2$), which occurs along the axisymmetric resonance line (ARL) in (L_z, J_R) , to identify in the *Gaia* action data three candidates for the bar’s OLR and pattern speed Ω_{bar} : $1.85\Omega_0$, $1.20\Omega_0$, and $1.63\Omega_0$ (with $\sim 0.1\Omega_0$ systematic uncertainty). The *Gaia* data is therefore consistent with both slow and fast bar models in the literature, but disagrees with recent measurements of $\sim 1.45\Omega_0$. (2.) For the first time, we demonstrate that bar resonances—especially the OLR—cause a gradient in vertical action $\langle J_z \rangle$ with L_z around the ARL via “ J_z -sorting” of stars. This could contribute to the observed coupling of $\langle v_R \rangle$ and $\langle |v_z| \rangle$ in the Galactic disc. (3.) We confirm prior results that the behaviour of resonant orbits is well approximated by scattering and oscillation in (L_z, J_R) along a slope $\Delta J_R / \Delta L_z = l/m$ centered on the $l:m$ ARL. Overall, we demonstrate that axisymmetrically estimated actions are a powerful diagnostic tool even in non-axisymmetric systems.

Key words: Galaxy: disc – Galaxy: kinematics and dynamics

1 INTRODUCTION

1.1 Moving groups and bar resonances

In the local Solar neighbourhood (~ 200 pc) of the pre-*Gaia* era, stellar moving groups have been identified in both the stars’ velocities (e.g., Eggen 1996; Dehnen 1998; Famaey et al. 2005) and orbit space (e.g., Arifyanto & Fuchs 2006; Klement et al. 2008). The amount of kinematic substructure in the in-plane motions of the Galactic disc stars discovered by the *Gaia* Collaboration et al. (2018b) in the radial velocity sample (RVS) of the second *Gaia* data release (DR2) (Gaia Collaboration et al. 2016, 2018a) was still surprising (c.f. Bovy et al. 2009). At least seven arches or ridges are visible in the (U, V) velocity space within $\sim 1.5 - 4$ kpc from the Sun (Gaia Collaboration et al. 2018b), in the (R, v_T) plane (Antoja et al. 2018; Kawata et al. 2018) or orbital action space (Trick et al. 2019, T19 hereafter).

Their origin is still largely unexplained. Early studies sug-

gested a star cluster origin (Eggen 1996; Chereul et al. 1998), which is however not supported by age-abundance measurements (Nordström et al. 2004; Bensby et al. 2007; Famaey et al. 2007, 2008). Several dynamic processes have been proposed that could cause these kinematic ridges: Spiral arms (Kalnajs 1991; Quillen 2003; De Simone et al. 2004; Quillen & Minchev 2005; Sellwood 2012; Quillen et al. 2018; Kawata et al. 2018; Sellwood et al. 2019; Khoperskov et al. 2020) and bar resonances (e.g., Dehnen 2000; Fux 2001; Fragkoudi et al. 2019, 2020), secular evolution of the disc in general (e.g., Sellwood 2012; Fouvy et al. 2015b,c; going back to Toomre 1981) and transient processes like phase-mixing caused by transient spiral structure (Fouvy & Pichon 2015; Hunt et al. 2018) and satellite interactions (Minchev et al. 2009; Gómez et al. 2012; Antoja et al. 2018; Laporte et al. 2019; Khanna et al. 2019).

Resonance effects in particular have been studied in depth in the literature (see Minchev (2016) for a pedagogical introduction). A star’s orbit experiences lasting changes if its fundamental frequencies are commensurate with the pattern speed of the periodic perturber, Ω_{bar} . In other words, the radial frequency with which

* E-mail: trick@mpa-garching.mpg.de

the star oscillates in the radial direction, $\Omega_{R,\text{true}}$, and the circular frequency around the Galactic center, $\Omega_{\phi,\text{true}}$, (Binney & Tremaine 2008, §3.2.3) are related with the pattern speed of the bar by

$$m \cdot (\Omega_{\text{bar}} - \Omega_{\phi,\text{true}}) - l \cdot \Omega_{R,\text{true}} = 0, \quad (1)$$

with $m, l \in \mathbb{Z}$. At $l = 0$, the star is in co-rotation resonance (CR) with the bar. $l > 0$ describes resonances outside, and $l < 0$ resonances inside of CR in the Galactic disc. Depending on the mass distribution of the perturber, the resonances at different m have different strength. The $m = 2$ Fourier component of a typical galaxy bar is dominant (Buta et al. 2006), so its $l = \pm 1$, $m = 2$ resonances, the Outer and Inner Lindblad Resonances (OLR and ILR), are expected to have a strong effect on the Galactic disc.

In the pre-*Gaia* era, many studies focused on explaining the Hercules stream with bar resonances. The *short fast bar* model with $\Omega_{\text{bar}} \sim 51$ km/s/kpc associates Hercules with the OLR signature of the bar (Dehnen 2000; Chakrabarty 2007; Minchev et al. 2007; Antoja et al. 2014; Monari et al. 2017b,a; Minchev et al. 2010; Fragkouidi et al. 2019). Recent evidence from gas and stellar structures in the inner Galaxy converges, however, on $\Omega_{\text{bar}} \sim 40$ km/s/kpc (e.g. Rodriguez-Fernandez & Combes 2008; Long et al. 2013; Sormani et al. 2015; Portail et al. 2017; Sanders et al. 2019; Clarke et al. 2019; Bovy et al. 2019). Depending on the Milky Way (MW) rotation curve, this explains the Hercules stream either by CR (the *long slow bar*; Pérez-Villegas et al. 2017; Monari et al. 2019a; D’Onghia & L. Aguerrí 2020) or the 1:4 resonance (*slightly faster slow bar*; Hunt & Bovy 2018). (More details in Section 6.3.)

Action space has proven to be especially powerful to study resonance effects (e.g. Lynden-Bell & Kalnajs 1972; Arnold 1978; Martinet et al. 1981; Rauch & Tremaine 1996; Sellwood 2012). Strategies include the calculation of the so-called slow and fast actions for a given, individual resonance region (e.g., Lynden-Bell 1979; Fouvy & Pichon 2015; Monari et al. 2017c), or the perturbation of action-based distribution functions (e.g., Sellwood & Lin 1989; Fouvy et al. 2015a; Fouvy & Pichon 2015; Fouvy et al. 2015d; Monari et al. 2016a, 2017a), or the perturbation of the orbital tori themselves (Binney 2018, 2020a).

1.2 Axisymmetric action and frequency estimates as a diagnostic tool

The *true actions* are true integrals of motion. For general gravitational potentials, it is however not always known how to calculate them, or (all three) actions might not even exist. The *axisymmetric actions* $\mathbf{J} \equiv (J_R, J_\phi, J_z)$ are integrals of motion in some static, axisymmetric potentials, but not conserved in more general galaxy potentials with bars and/or spiral arms. Using a best-fit model for the background axisymmetric potential of the MW (e.g. McMillan 2011a; Bovy 2015; Eilers et al. 2019), we can still calculate instantaneous *axisymmetric action estimates* \mathbf{J} from observed stellar positions and velocities, with the azimuthal action $J_\phi = R \cdot v_T \equiv L_z$ being the z-component of the angular momentum.

In an axisymmetric potential Φ_{axi} , an orbit has the fundamental frequencies

$$\Omega_{i,\text{axi}}(\mathbf{J}) \equiv \frac{\partial \mathcal{H}_{\text{axi}}(\mathbf{J})}{\partial J_i} \quad (2)$$

with $i \in [R, \phi, z]$ denoting the Galactocentric cylindrical coordinates, where \mathcal{H}_{axi} is the Hamiltonian of the axisymmetric system (see, e.g., Binney & Tremaine 2008, §3.5). These frequencies describe the oscillation a star on a given orbit \mathbf{J} experiences in the three coordinate directions. An in-plane rosette-like disc orbit, for

example, can be considered as a superposition of (i) a circular orbit with the (guiding-center) radius $R_g(L_z|\Phi_{\text{axi}})$ and (ii) an epicycle. The guiding-center of the epicycle moves along the circular orbit with frequency $\Omega_{\phi,\text{axi}}$. In the axisymmetric limit, $\Omega_{\text{axi}} = \Omega_{\text{true}}$. The star moves around the epicycle with frequency $\Omega_{R,\text{axi}}$. The larger the radial action J_R , the more extended is the radial oscillation amplitude of the orbit’s rosette. Even though the axisymmetric disc model does not contain a bar, we set up a resonance condition¹ analogous to Equation (1) using these axisymmetric frequencies:

$$m \cdot (\Omega_{\text{bar}} - \Omega_{\phi,\text{axi}}) - l \cdot \Omega_{R,\text{axi}} = 0 \quad (3)$$

For a given (l, m) and Ω_{bar} , we can identify those stars with zero vertical excursions, $J_z = 0$, that satisfy this condition. In action space (L_z, J_R) , these stars lie along a line. We call this resonance line the *axisymmetric resonance line* (ARL) for short as it is calculated on the basis of axisymmetric action and frequency estimates. It was first plotted by Sellwood (2010) and also used in, e.g., Binney (2018). To construct ARLs, we do not require any knowledge about or the existence of a perturber—except for an assumed value for Ω_{bar} . In practice, we find the ARL by fitting a linear line to simulation particles with $J_R < 0.15L_{z,0}$ and $J_z < 0.001L_{z,0}$ for which Equation (3) is satisfied.

ARLs have a negative slope in the (L_z, J_R) plane (Sellwood 2010). For studies of resonances in position-velocity coordinates this means that the exact Galactocentric radius R (related to L_z) at which the resonance condition is satisfied depends on the eccentricity of the orbit (related to J_R). A resonance spans therefore a whole region in R , the “Lindblad zone”, as shown by Struck (2015).

In the pre-*Gaia* era, dynamic effects could only be studied locally (< 200 pc from the Sun) where velocities stand in for orbit labels. In the extended RVS sample of *Gaia* DR2, larger parts of an orbit are captured; velocities change along the orbit while integrals of motion stay (roughly) constant. They are therefore better suited to characterize different orbits across the Galaxy. The classical integrals—the total energy E together with L_z —are for example often used to find orbit substructure in the Galactic halo (e.g. Helmi et al. 1999, 2017; Gómez et al. 2010; Koppelman et al. 2018; Myeong et al. 2018). The main advantage of the action integrals is that they are conserved during adiabatic changes of the (axisymmetric) gravitational potential. Their intuitive meaning and the convenient properties of the canonical action-angle coordinate space make them our integrals of choice.

In this work, we investigate if axisymmetric action and frequency estimates can be informative about the unknown non-axisymmetries in the MW, as also suggested in earlier work by Binney (2018), Sellwood (2010), and others.

One goal of Galactic Dynamics is to perform *quantitative* dynamical modelling of the *Gaia* data, including bar and spiral arms. Several authors (e.g., Binney & Tremaine 2008; Rix & Bovy 2013) advocate to first strive for an axisymmetric dynamical model of the MW (e.g. as in Trick et al. 2017), in which the effect of non-axisymmetries can subsequently be included using quasi-linear

¹ At many time steps along a bar-affected orbit, $\Omega_{\text{true}} \neq \Omega_{\text{axi}}$. A star can be either a resonantly trapped orbit and *always* satisfy Equation (1), or a non-resonant, circulating orbit that *never* satisfies Equation (1). The former *will* sometimes satisfy Equation (3), i.e., when it just crosses the ARL. The latter *may* sometimes cross the ARL and thus temporarily satisfy Equation (3), depending on how close the star lives on average to the resonance, and how much it oscillates in action space. This is a consequence of Ω_{axi} being a ‘wrong’ local estimate. The above described behaviour in action space will become clear later on in Section 4 and Appendix B.

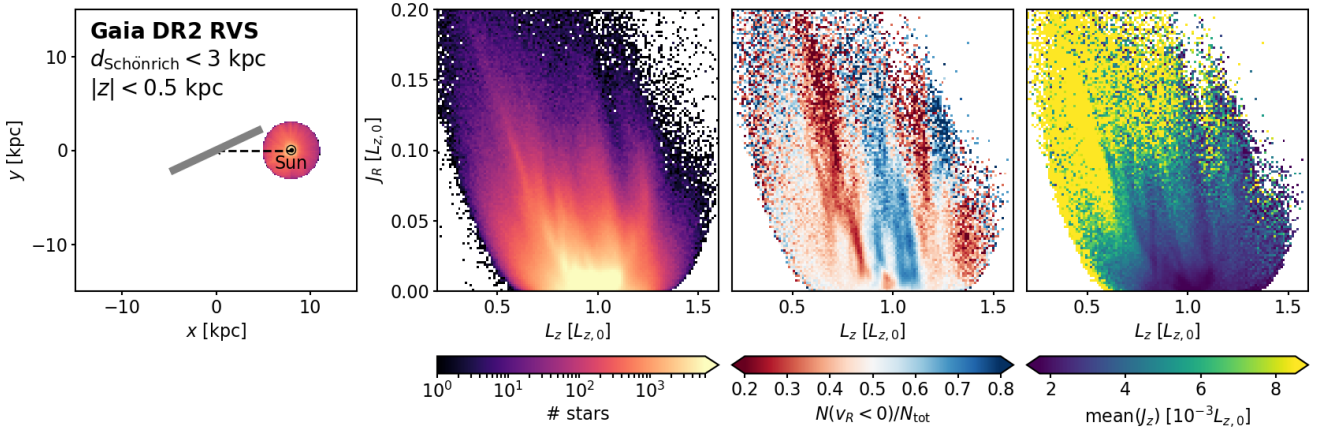


Figure 1. *Gaia* DR2 RVS data in axisymmetric action space estimated in the MWPotential2014. To summarize the main findings in T19, we show the stellar density, the v_R -asymmetry and the mean vertical action $\langle J_z \rangle$ as a function of the in-plane actions (L_z, J_R) . As opposed to T19, we use the distances by Schönrich et al. (2019) and show the action distribution within the larger volume of $d_{\text{Schönrich}} < 3$ kpc. The actions are given in units of $L_{z,0} = 8 \text{ kpc} \times 220 \text{ km/s}$. Overdensity ridges are related to stripes of predominantly inward- (blue) or outward (red) motions, and on average low J_z .

perturbation theory (Kalnajs 1971; Weinberg 2001; Fouvy et al. 2015d; Monari et al. 2016a, 2017c; Binney 2018). However, the sheer amount of substructure in the *Gaia* data requires that we first *qualitatively* disentangle the mechanisms creating the individual ridges.

It has been shown that very different bar and spiral arm models can be tuned to look like the local *Gaia* data (Hunt et al. 2019) or convincingly explain all observed features at once (e.g. Monari et al. 2019a; Khoperskov et al. 2020; Chiba et al. 2019). Complex models with many free parameters face therefore—at least at this point in time—the Münchhausen trilemma.² Different strategies can mitigate this problem. Firstly, external information can be employed as a prior to constrain some degrees of freedom, e.g., by using existing bar models based on Galactic center data (Portail et al. 2017) to model local disk data (Monari et al. 2019a). Secondly, covering a larger region in the 6D phase-space, with observations and in the modelling, increases the information content available in the data; Monari et al. (2019a) and Hunt et al. (2019) study, for example, different 2D and 3D projections of the 4D in-plane phase-space.

The chosen approach in this work inverts the first strategy. We present a detailed exploration of *just one* strong perturbing mechanism in the Galactic disc: the $m = 2$ resonances of the bar with a constant pattern speed. By building intuition about its signatures in the space of axisymmetric actions, the *Gaia* data *alone* might reveal candidates for the bar’s true OLR. These ‘uninformed’ results are subsequently compared to external information from other studies. Agreement should then make the identification of the remaining features observed in the Galactic disk and their respective perturbers easier. Discrepancies should be used to inform us with respect to which parts of the OLR signature the simple bar model requires modification and more complexity.

Concerning the second strategy, we use *Gaia* data within 3 kpc from the Sun and study them in three in-plane dimensions, (J_R, L_z)

and the radial phase proxy v_R , and—for the first time—also in one out-of-plane dimension, the vertical action J_z . In this work, we do not cover the fourth in-plane dimension, i.e., the Galactocentric azimuth ϕ or the related orbital tangential phase-angle θ_ϕ . A companion study, investigating the resonance signatures in the space of orbital phase-angles, is currently in preparation.

This paper is organized as follows. In Sections 2 and 3, we present the *Gaia* DR2 action data and the test particle simulation of a barred galaxy. Section 4 recapitulates the background theory of bar resonances by means of numerically integrated orbits in action space. Readers who are already familiar with resonant phenomena in action space are encouraged to skip to Section 5 where we lay out our main results: In Section 5.1, we demonstrate how the OLR signature in action space can be used to estimate the bar’s pattern speed from the *Gaia* data; in Section 5.2, we show how resonances affect the distribution of the vertical action J_z . In Section 6, we investigate the proposed bar pattern speeds more closely and discuss them with respect to existing models in the literature. We summarize and conclude in Section 7.

2 DATA

We use the *Gaia* DR2 action data introduced in T19. For distances larger than ~ 1 kpc, the inverse parallax as employed by T19 is a poor distance measurement. In this work, we therefore use instead the $(\alpha, \delta, \mu_\alpha^*, \mu_\delta, v_{\text{los}})$ from *Gaia* DR2 RVS (Gaia Collaboration et al. 2016, 2018a; Katz et al. 2019) together with the Bayesian distance estimates by Schönrich et al. (2019) that include a systematic parallax offset of 0.048 mas. This allows us to use the *Gaia* action data out to $d = 3$ kpc from the Sun. In addition, we restrict the data to within $|z| = 500$ pc from the Galactic plane and do not apply any quality cuts, as discussed in T19. This data set includes ~ 4.8 Million stars.

In Figure 1, we show the corresponding axisymmetric action estimates in the MWPotential2014 model by Bovy (2015), with the (L_z, J_R) distribution colour-coded by stellar density, v_R -asymmetry, and $\langle J_z \rangle$, thus summarizing the three main findings by T19:

- (i) The *stellar overdensities* in the in-plane velocity space are

² Any model that reproduces all the substructure in the *Gaia* data can only be considered as truth, if also the model assumptions (e.g. about the many mechanisms involved, the bar, spiral arms, and satellite interactions) themselves are close to the truth.

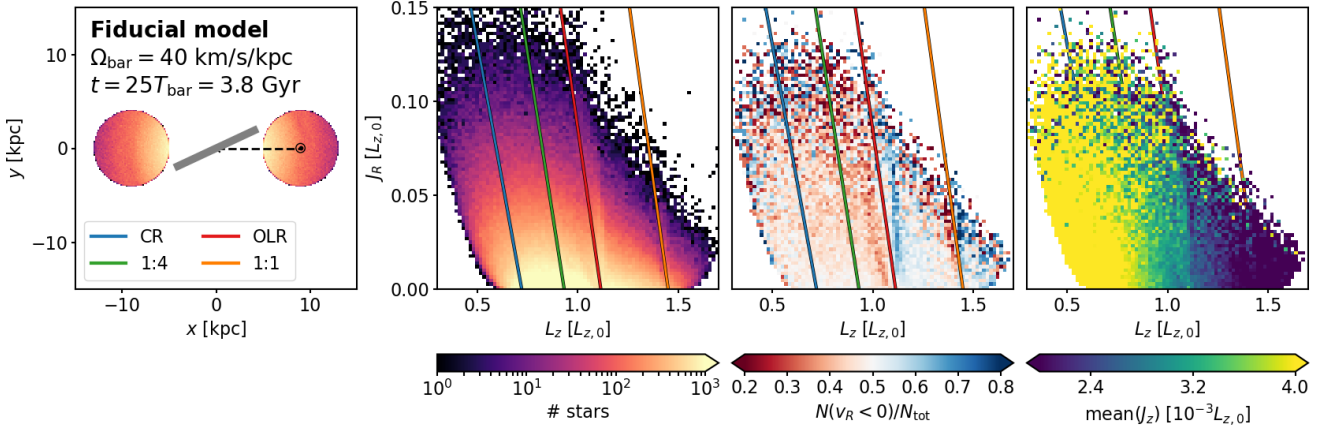


Figure 2. Axisymmetric action space for the test particle simulation in the Fiducial bar model in a *Gaia*-like survey volume (cylinder with radius 4 kpc and $|z| < 500$ pc around a solar-like position at $R = 9$ kpc). This figure shows the location of the survey volume with respect to the bar (after $t = 25T_{\text{bar}} = 3.8$ Gyr of orbit integration), the stellar number density in the (L_z, J_R) plane, as well as action space colour-coded by the number of inward moving stars ($v_R < 0$) to the total number of stars (N_{tot}) per bin and the mean vertical action $\langle J_z \rangle$. We overplot the ARLs for $\Omega_{\text{bar}} = 40$ km/s/kpc. The signatures caused by the OLR and 1:1 resonance resemble qualitatively some of the features observed in the *Gaia* data in Figure 1.

the local manifestation of an extended system of orbit structures in the Galactic disc which reach consistently out to (at least) ~ 3 kpc from the Sun and lie along ridges of slightly negative slopes $\Delta J_R / \Delta L_z$ around $L_z \sim \text{const}$.

(ii) Action space colour-coded by the fraction of inward-moving stars, reveals a strong v_R -asymmetry pattern of predominantly inward- or outward motion along the ridges. This corresponds to asymmetric numbers of stars at $+v_R$ vs. $-v_R$ in the well-known $(U, V) \sim (-v_R, v_T - v_{\text{circ}})$ plane of the Solar neighbourhood. In some recent papers, the same features were shown by Fragkoudi et al. (2019) and Laporte et al. (2019), who colour-coded the (R, v_T) plane by $\langle v_R \rangle$, and by Friske & Schönrich (2019), who plotted $-v_R$ as a function of L_z and in the (L_z, ϕ) plane.

(iii) Another property of action space found in T19 was that the overdensity ridges were related to on average low vertical action J_z . Khanna et al. (2019) also noted that the ridges in (R, v_T) live mostly at low $|z|$.

Any proposed creation mechanism for the ridges needs to be able to explain all three of these properties.

3 SIMULATION

3.1 Test particle simulation

Simulation setup.—To investigate the effect of the bar on individual orbits in action space, we set up an idealized MW-like galaxy test particle simulation. The initially axisymmetric galaxy uses the MWPotential2014 as the gravitational background potential (with $R_0 \equiv 8$ kpc, $v_0 \equiv v_{\text{circ}}(R_0) = 220$ km/s, $L_{z,0} \equiv R_0 \times v_0 = 1760$ kpc km/s, and $\Omega_0 \equiv v_0/R_0 = 27.5$ km/s/kpc). We generate a stellar disc with 5 Million massless test particles from the quasi-isothermal distribution function (DF) by Binney & McMillan (2011). Then, we add the 3D quadrupole ($m = 2$) bar model by Dehnen (2000) and Monari et al. (2016b) to the potential, orientated at an azimuth of 25 degrees with respect to and ahead of the Sun (Bovy et al. 2019), and rotate it with a pattern speed of $\Omega_{\text{bar}} = 40$ km/s/kpc $= 1.45\Omega_0$. Our Fiducial bar model has a weak bar strength. Its pattern speed was chosen for illustration purposes and is only by coincidence close to the (slightly faster) slow

bar pattern speed in the literature. We integrate the orbits of all mock stars in the barred potential for up to 25-50 bar periods using galpy³. Their final phase space coordinates (\mathbf{x}, \mathbf{v}) are then used to estimate the actions \mathbf{J} and frequencies Ω_{axi} in the axisymmetric background MWPotential2014 using the *Stäckel Fudge* algorithm by Binney (2012) (Bovy & Rix 2013; Sanders & Binney 2016). The model parameters of the Fiducial bar model are summarized in Table 1. In Appendix C, we present more details about the simulation setup, and illustrate it in Figure C1.

Methodological context to related and recent studies.—A similar study using the idealized test particle simulation approach was performed by Mühlbauer & Dehnen (2003). They investigated bar resonances in the velocity moments as a function of R at $z = 0$. We are interested in action space (L_z, J_R) and use a 3D bar to study also signatures in J_z . Binney (2018) investigated the DF in (L_z, J_R) evolving under the influence of a bar by applying perturbation theory. To be able to interpret action-angle space of Galactic surveys, correcting for selection effects is crucial (McMillan 2011b). Combining selection functions with perturbed action-angle-based DFs is non-trivial, so we resort to test particle simulations. Monari et al. (2019a), Hunt et al. (2019), and Sellwood et al. (2019) studied the signatures of bars and/or spiral arms in action space at fixed positions in the Galaxy using the backwards-integration method by Dehnen (2000). This method finely resolves the ridges, but becomes noisy when integrating for more than ~ 10 bar periods. Fragkoudi et al. (2019) and Hunt et al. (2019) studied resonance signatures in self-consistent N-body and test particle simulations with more complex bar models, respectively. To complement these studies, we focus here on isolating and describing the effect of the $m = 2$ bar only.

Parameter space exploration.—We have run test particle simulations with different (a) pattern speeds, (b) integration times, (c) bar strengths, (d) either slowly introducing the bar over several bar periods or switching it on instantaneously, (e) including different $m = 4$ bar components. The behaviour of tests (a)-(d) was well-behaved

³ The Python package for Galactic dynamics galpy by Bovy (2015) can be found at <http://github.com/jobovy/galpy>.

for weak bars, as expected when comparing to our Fiducial bar model, and left the results in this work qualitatively unchanged. We therefore focus on the Fiducial model only. Adding the $m = 4$ bar component in tests (e) confirmed the findings by Hunt & Bovy (2018) and Monari et al. (2019a) in some respects (see Section 6.1), and disagreed in others. It increased the space of bar parameters to explore and introduced complex behaviour. The signatures of the $m = 2$ component, however, remained very similar. A detailed discussion of the effect of the $m = 4$ components is therefore beyond the scope of this paper.

3.2 Action space of the Fiducial model around the Sun

In Figure 2, we show the action distribution analogously to the *Gaia* data for the Fiducial bar model for test particle stars within the two cylinders of radius 4 kpc centered on an observer’s position at $(x, y, z)_\odot = (\pm 9, 0, 0)$ kpc. By using the frequencies $(\Omega_R, \Omega_\phi)_{\text{axi}}$, we overplot the ARLs for the known Ω_{bar} of the system.

In the stellar density distribution, we note (i) an high- J_R overdensity ridge to the right (and an underdensity region to the left) of the OLR and 1:1 ARL, as expected (see Section 4.2), (ii) an otherwise smooth distribution similar to an axisymmetric distribution (c.f. Figure C1(b)), which is—except for the parabolic lower envelope⁴—(iii) very similar to the action space without any spatial subselection (c.f. Figure C1(e)). The latter is one of the advantages of using action space.

The v_R -asymmetry panel in Figure 2 shows that the ARL of the OLR (and also the 1:1 ARL) separates an outward-moving (red) stripe from an inward-moving (blue) stripe. In addition, there is a weak trend towards outward-moving (red) stars for L_z smaller than the OLR. We will investigate this OLR signature in more detail in Section 5.1.

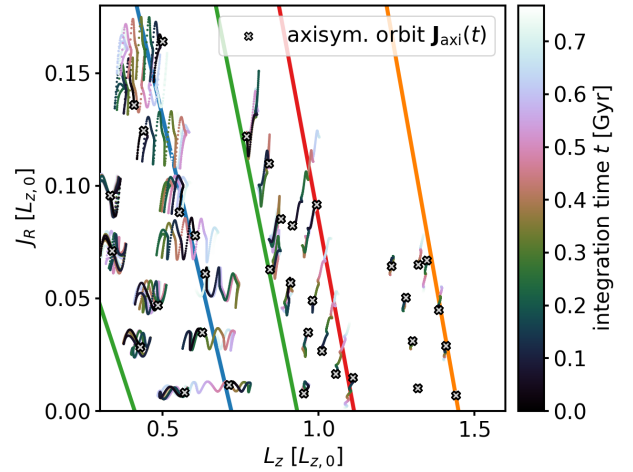
The mean vertical action in Figure 2 shows the expected trend of decreasing $\langle J_z \rangle$ with L_z . The reason is that orbits with the same z_{max} (i.e., maximum height above the plane that can be reached), have higher J_z if they live in the inner disk because of the higher surface-mass density. Interestingly, this trend is broken around the OLR: The underdensity region to the left of the OLR has higher $\langle J_z \rangle$ while the overdensity ridge to the right of the OLR resonance has lower $\langle J_z \rangle$. This is surprising, as the bar potential model depends on z only very weakly in the Solar vicinity, and the J_z of the individual stars did not change significantly during orbit integration; the mean change is just $\langle |J_{z,\text{end}} - J_{z,\text{start}}| \rangle / L_{z,0} \sim 4 \cdot 10^{-5}$. We will investigate this further in Section 5.2.

Overall, Figure 2 illustrates that bar resonances, in particular the OLR, can give rise to signatures in the space of axisymmetric actions qualitatively similar to some of those observed in the *Gaia* data.

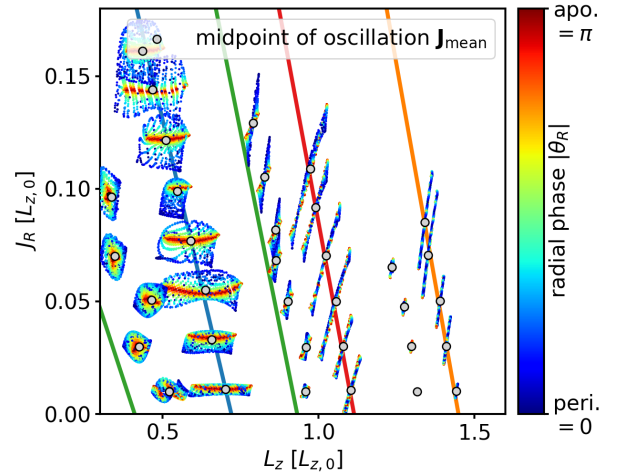
4 BACKGROUND

4.1 Numerical example orbits in action space

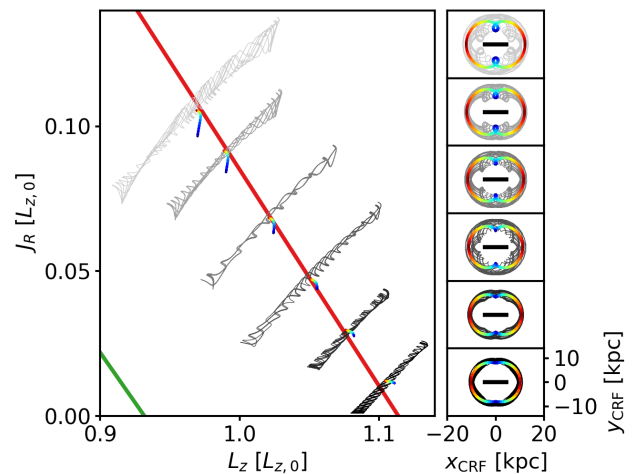
The behaviour of bar-affected orbits in action space has often been studied on the basis of perturbation theory. (A recent and pedagogical explanation can be found, for example, in Chiba et al. (2019).) To complement this, we show here numerically integrated orbits in



(a) Action evolution of bar-affected orbits versus the corresponding orbit in the axisymmetric potential for an integration time of $5T_{\text{bar}} = 0.8$ Gyr.



(b) For an integration time of $50T_{\text{bar}} = 7.7$ Gyr, all stars reveal an oscillation in axisymmetric action space. Resonant orbits oscillate around their ARL. The colour-coding according to peri-/apocenter illustrates the orbit libration.



(c) OLR orbits only, in action space (left) and in the (x, y) frame (right) co-rotating with the bar (black). The librating orbits are shown in grey, their corresponding closed parent orbits are colour-coded by radial phase.

⁴ The parabolic envelope at low J_R in the action distribution is due to the cylindrical selection of the data. See §2.3.2 in T19 for an explanation of this selection effect.

Figure 3. Example orbits integrated in the Fiducial bar potential and their time evolution in the axisymmetric (L_z, J_R) action plane. The thick solid lines are the CR (blue), OLR (red), 1:1 (orange), $\pm 1:4$ (green) ARLs. We show both resonant stars and stars in-between the ARLs.

the space of axisymmetric actions. We start with a few individual examples in Figure 3 to build intuition.

Figure 3(a) shows (as grey crosses) the orbits integrated in the axisymmetric `MWPotential2014` for an integration time of $t = 5T_{\text{bar}} = 0.8$ Gyr. As the actions are conserved in this potential, the time evolution along each orbit corresponds to one single point $J_{\text{axi}}(t) = \text{constant}$. Inaccuracies in the orbit integration and action estimation do lead to small (unphysical) time variations in \mathbf{J}_{axi} , but they are smaller than the marker size in Figure 3(a).

If we integrate the stars with the same initial conditions in the potential with the rotating bar, they all move substantially in both L_z and J_R direction (colour-coded by time in Figure 3(a)).

Figure 3(b) shows the same orbits for a longer integration time of $t = 50T_{\text{bar}} = 7.7$ Gyr. All stars oscillate in a restricted area within (L_z, J_R) . We take the time-average to determine the central location around which the orbit oscillates (marked by a grey dot), i.e.,

$$\mathbf{J}_{\text{mean}} \equiv \langle \mathbf{J}(t) \rangle_t. \quad (4)$$

In the following, we discuss the resonant phenomena of *scattering*, *libration around parent orbits*, *oscillation*, and *orbit orientation* by means of these numerical orbits in action space and knowledge from the literature. We explain how they lead to the signatures observed in Figure 2.

4.2 Scattering

It has long been known that *resonant scattering* can change orbits substantially (Lynden-Bell & Kalnajs 1972). Sellwood & Lin (1989) for example showed that resonant scattering at spiral arms creates ridges in action space (their fig. 7). A rotating bar potential with a fixed pattern speed conserves the Jacobi integral

$$E_J = E - \Omega_{\text{bar}} \times L_z \quad (5)$$

along a star's orbit (Binney & Tremaine 2008, §3.3.2). Sellwood & Binney (2002) demonstrated analytically that this implies the following relation:

$$\Delta J_R = \frac{\Omega_{\text{bar}} - \Omega_\phi}{\Omega_R} \Delta L_z = \frac{l}{m} \Delta L_z. \quad (6)$$

This relation is valid in the epicyclic approximation of near circular orbits and still approximately true for more eccentric orbits (Lynden-Bell & Kalnajs 1972; Sellwood & Binney 2002). We illustrate this scattering process due to bar resonances, which changes a star's long-term average location \mathbf{J}_{mean} with respect to its initial axisymmetric actions \mathbf{J}_{axi} , by plotting in Figure 4 the difference

$$\Delta \mathbf{J} \equiv \mathbf{J}_{\text{mean}} - \mathbf{J}_{\text{axi}}. \quad (7)$$

ΔL_z describes an average, lasting change in L_z due to the bar and contributes to the radial migration of stars within the disk. ΔJ_R can be considered as a difference in the average amount of radial oscillation that the orbit experiences with respect to the unperturbed orbit. In Figure 4, we overplot also...

- (i) ...stars that are according to Equation (1) truly in resonance with the bar.⁵ It is therefore the stars in main resonances that experience substantial scattering (the extended wings with $|\Delta \mathbf{J}| \gg 0$ in Figure 4).

⁵ We determine the real fundamental frequencies of the orbits, $(\Omega_\phi, \Omega_R)_{\text{true}}$, from a Fourier analysis of $\mathbf{x}(t)$ analogous to Fragkoudi et al. (2019) (see also Binney & Spergel 1982; Laskar 1993).

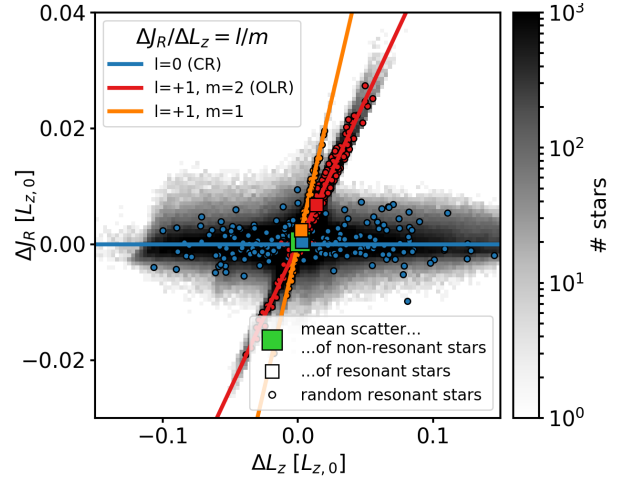


Figure 4. Scattering of all test particle stars with $R_{\text{end}} > 5$ kpc in the Fiducial bar simulation. “Scattering” is the lasting, average change in the axisymmetric action due to the bar (Equation (7)). The majority of stars with significant scattering, $|\Delta \mathbf{J}| \gg 0$, are as expected stars in resonance with the bar. As predicted by E_J conservation, resonant stars change their actions along $\Delta J_R / \Delta L_z \sim l/m$ (Sellwood & Binney 2002). A strong net change occurs at the OLR and 1:1 resonance (red and orange squares)

- (ii) ...the analytic scattering relation (6). As expected, the resonant scattering wings lie along slopes of

$$\Delta J_R / \Delta L_z \sim l/m. \quad (8)$$

The exact scattering direction depends on the star's instantaneous phase angles at the time the bar is switched on. If the bar in the simulation is slowly grown, the resonant stars follow the scattering relation more closely. In a test particle simulation with a stronger bar ($\alpha_{m=2} = 0.015$), stars can get scattered further.

- (iii) ...separately the average net change for all stars at a given resonance, and also for all non-resonant stars. We find that only at the OLR resonance occurs a significant *net* change in both L_z and J_R . As can also be seen in Figure 3(a), more stars at the OLR get scattered towards higher L_z than towards lower L_z .

The latter is a consequence of relation (6), which couples at the OLR and 1:1 resonance the direction of ΔL_z to the change in J_R . Stars with the same \mathbf{J}_{mean} got scattered from their initial \mathbf{J}_{axi} : either from higher $J_{R,\text{axi}}$ on the right of the ARL downwards, $\Delta L_z = 2\Delta J_R < 0$, or from lower $J_{R,\text{axi}}$ on the left upwards, $\Delta L_z = 2\Delta J_R > 0$. In the overall disk population, the stellar density decreases steeply with increasing J_R , i.e., many more stars live initially at lower $J_{R,\text{axi}}$. Consequently, scattering in the $\Delta L_z = 2\Delta J_R > 0$ direction occurs more often than in the opposite direction. In addition, near-circular orbits with $J_{R,\text{axi}} \sim 0$ can only increase their radial oscillations and therefore L_z . This is also illustrated in the (L_z, E) plane by fig. 1 in Sellwood & Binney (2002). Overall, this process leads to the underdensity vs. overdensity signature around the OLR and 1:1 resonances in Figure 2.

The strongest radial migration is, as expected, observed for individual CR stars. The CR's weak effect on J_R and the absence of a preferred scattering direction in L_z explains the absence of

obvious substructure around the CR ARL in Figure 2 (see also Appendix B).⁶

4.3 Parent orbits

In the axisymmetric system, rosette-shaped disk orbits can be grouped into families with the closed, circular orbit ($J_R = 0$) as the parent orbit. Orbits with the same L_z oscillate in the (R, v_R) plane around it—the larger J_R , the larger the amplitude.

In the barred system, resonant orbit families are grouped by the same E_J . Their parent orbits close in the $(x_{\text{CRF}}, y_{\text{CRF}})$ frame co-rotating with the bar and correspond to a point in the surface of section $(x_{\text{CRF}}, v_{x,\text{CRF}} | y_{\text{CRF}} = 0)$. In our mock simulation, the parent orbits do not get populated. We therefore use the algorithm by Sellwood & Wilkinson (1993) to determine the parent orbits belonging to the specific OLR example orbits in Figure 3. Figure 3(c) shows these parent orbits both in the co-rotating $(x_{\text{CRF}}, y_{\text{CRF}})$ frame and in action space. The parent orbits oscillate between peri- and apocenter which correspond to slightly different locations in (L_z, J_R) but constant E_J . This fast oscillation between the radial phases is in the literature described by the radial angle θ_R , also called the *fast angle* θ_f close to a resonance.

4.4 Libration

In perturbation theory studies, the orbit evolution is usually averaged over θ_f . It follows from E_J conservation that, on average, the quantity

$$J_f \equiv J_R - \frac{l}{m} L_z \sim \text{const.} \quad (9)$$

is close to an integral of motion. It is known in the literature as the *fast action* of a given resonance (see also Lynden-Bell 1979; Kaasalainen 1994; Weinberg 1994; Monari et al. 2017c).

In our numeric study using axisymmetric estimates, we observed in Figure 3(b) that the apocenter of each orbit changes with time along a line in (L_z, J_R) . This line is not perfectly linear. We have, however, checked in our simulation that the apocenters of true resonant stars at the main resonances (OLR, 1:1, CR, and also 1:4) move indeed along slopes

$$\delta J_R / \delta L_z \sim l/m, \quad (10)$$

where δJ_i is the oscillation amplitude in the J_i -direction (Equation (B1); see also fig. 4 in Binney 2018). (From Figure 3(b) it appears that the pericenters oscillate more strongly in action space.) The slow evolution along constant J_f is called *orbit libration* and the variation is described by the *slow angle* θ_s . Parent orbits do not librate (see Figure 3(c)). In the $(x_{\text{CRF}}, y_{\text{CRF}})$ frame co-rotating with the bar, the libration corresponds to the slow shift of the peri-/apocenter in azimuth ϕ_{CRF} . The azimuthal range within which the peri-/apocenters librate is restricted—this is called the *trapping* of

⁶ The scattering relation in Equation (6) is only satisfied in potential models with a fixed bar pattern speed. A recent study by Halle et al. (2018) investigated the net change in angular momentum at CR. They found that in their galaxy simulations which consider a realistic, self-consistent bar formation process including growth and slow-down, the CR swipes through a large range of Galactocentric radii and pulls trapped stars along, causing a large L_z net change. This radial migration of the stars due to the transient process is called “churning”. For a fixed potential with constant pattern speed, they did not measure a L_z net change, just periodic oscillations around CR, as in our Figure 3.

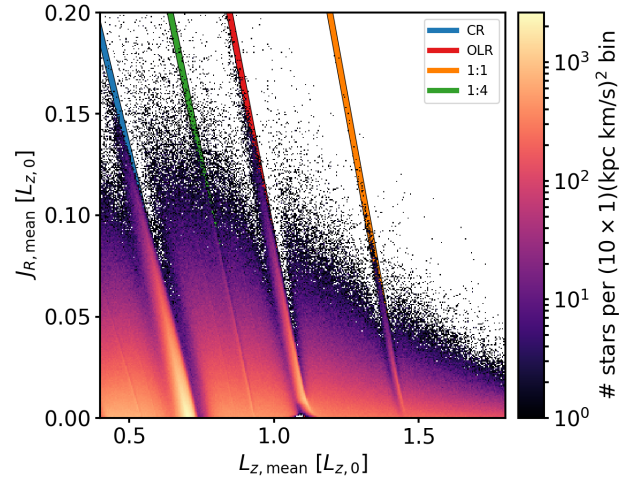


Figure 5. Oscillation midpoints \mathbf{J}_{mean} in the fiducial bar model. We define “oscillation” as the midpoint \mathbf{J}_{mean} and the amplitudes δJ_R and δL_z (see Figure B1) with which the stars oscillate around it in the plane of axisymmetric actions (see Figure 3(b)). This figure illustrates a “trapping” of stars at the resonances: The distribution of oscillation midpoints is smooth in the actions (L_z, J_R) , only the vicinity of the ARLs gets depleted and stars accumulate along the $l : m$ ARLs.

the orbit at the resonance (see, e.g., the OLR example orbits in Figure 3(c), and fig. 1 and 6 in Monari et al. (2017c)).

The maximum libration amplitude possible at a resonance, depends on $J_{R,\text{mean}}$, and the strength of the bar. Beyond this boundary (called the *separatrix*), orbits are circulating, i.e. the whole azimuthal range $\phi_{\text{CRF}} \in [-\pi, \pi]$ is available to the peri-/apocenters. More details can be found in, e.g., Binney (2018); Chiba et al. (2019).

4.5 Oscillation

To summarize, a resonant orbit ‘swings’ fast between peri- and apocenter, and librates slowly along a line of average constant J_f . Our axisymmetric action estimates L_z and J_R oscillate in both cases—and also significantly along non-resonant orbits. In the following, we use the term *oscillation* therefore to describe the general variation in L_z or J_R , not just at the resonances. At the resonances, the idealized prediction in Equation (6) is a good approximation to describe the overall behaviour of scattering and oscillation.

In Figure 5, we show now the distribution of oscillation midpoints $(L_{z,\text{mean}}, J_{R,\text{mean}})$ for all mock stars in the fiducial model. We overplot the ARLs. Overall, the distribution looks smooth and similar to (L_z, J_R) , showing that most stars oscillate close to their \mathbf{J}_{axi} (i.e. scattering $\Delta \mathbf{J} \sim 0$). Only in the vicinity of the ARLs, the resonance has depleted regions of \mathbf{J}_{mean} and accumulated the stars’ oscillation midpoints along the ARLs.⁷ The stars that are trapped at the resonances librate around the ARLs, was also one of the main findings by Binney (2018) from the study of perturbed tori.

As laid out in Appendix B, all stars oscillate and, in general, the oscillation amplitude δJ_R increases with J_R , and δL_z decreases

⁷ In Figure 5, at high J_R , the stellar distribution in \mathbf{J}_{mean} tilts away from our linear ARL fit to stars satisfying Equation (3). This is because for $J_R > 0.15 L_{z,0}$, the ARL does actually not stay perfectly linear.

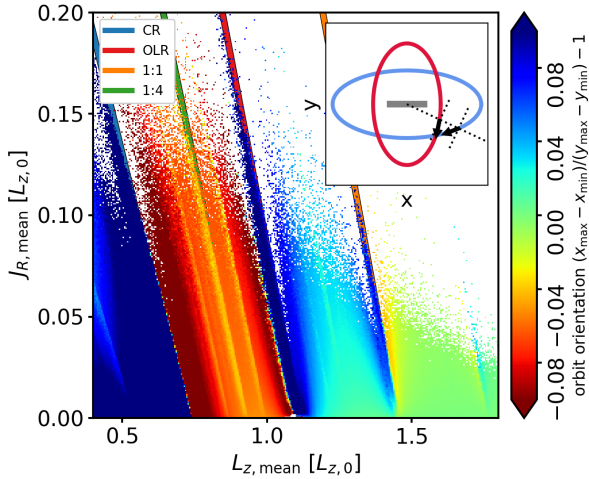


Figure 6. Orbit orientation in the frame co-rotating with the bar as a function of the oscillation midpoints in action space. For each orbit in the *Fiducial* simulation we get an estimate for the orbit elongation and its orientation as $q \equiv (x_{\max} - x_{\min}) / (y_{\max} - y_{\min}) - 1$, where $x = 0$ is always aligned with the bar (see inserted cartoon). For $q = 0$, the orbit appears round, for $q \neq 0$ elongated. For $q > 0$, the orbit is aligned with the bar. For $q < 0$ the orbit is anti-aligned with the bar. This figure illustrates that, when averaging the axisymmetric action estimates over time, these orbit orientation flips occur cleanly along the ARLs in action space. This is a consequence of the well-known fact that librating resonant orbits follow the underlying pattern of their parent orbits. Around the OLR, the orbit orientation flip translates into a velocity flip in the Solar neighbourhood (in the cartoon at an angle of $\phi_{\odot} = 25$ deg behind the bar).

with L_z . The resonances, in particular those with $l \neq 0$, are locations of increased J_R oscillation as expected (see Figure B1).

4.6 The orbit orientation flip at the OLR

Orbit orientation flips in the ‘time-averaged’ action-space.—It is well known that, in the $(x_{\text{CRF}}, y_{\text{CRF}})$ frame co-rotating with the bar, the orientation of orbits changes its direction at the principle resonances (see, e.g., Contopoulos & Grosbol 1989; Sellwood & Wilkinson 1993). At the OLR, the orbit orientation flips from anti-aligned inside of the OLR (the $x_1(2)$ orbit family) to being aligned with the bar outside of the OLR (the $x_1(1)$ orbit family). This was first discussed by Sanders & Huntley (1976) for gas particle orbits, and also by Kalnajs (1991). Dehnen (2000) illustrates this for stellar orbits.⁸

We found that these orbit orientation flips can be illustrated especially well in the action plane $(L_{z,\text{mean}}, J_{R,\text{mean}})$ of oscillation midpoints. The oscillation midpoints are quantities that we found as the time-average from integrating (part of) the whole orbit—in some sense they are therefore better “integrals of motion” or orbit labels than the instantaneous L_z and J_R , because the variation due to libration and radial oscillation is averaged out. From Figures 3(b)–3(c), we see that the oscillation midpoints of librating stars are close to their parent orbits in action space. In Figure 6, we plot for the *Fiducial* simulation in this plane the orbits’ orientation and elongation. This shows that the orbit orientation flip occurs cleanly along the OLR ARL in action space.

⁸ See, e.g., fig. 8 in Dehnen (2000), fig. 4 and 6 in Fux (2001), and fig. 5 in Fragkoudi et al. (2019) for an illustration of resonant orbit types.

Fragkoudi et al. (2019), using a self-consistent N -body simulation, demonstrated that in the region inside of the OLR ($L_z = R \times v_T \ll L_{z,\text{OLR}}$) the $x_1(2)$ orbit family overlaps with highly librating orbits from the $x_1(1)$ family. When comparing Figure 6 with the oscillation amplitude in Figure B1(a), we confirm this finding by Fragkoudi et al. (2019): In the (L_z, J_R) plane, the aligned OLR orbits ($q > 0$) librate strongly around the OLR ARL, while the anti-aligned orbits ($q < 0$) inside the ARL oscillate much less, leading to this orbit overlap inside the OLR ARL.

The OLR in velocity space.—A well-known consequence of the orbit orientation flip around the OLR is that at the Solar azimuth stellar radial velocities switch from outward-moving to inward-moving (see Dehnen 2000; Fux 2001; Mühlbauer & Dehnen 2003; Fragkoudi et al. 2019, and the cartoon insert in Figure 6). The bimodality of the pre-*Gaia* (U, V) velocity plane—the outward-moving Hercules stream around $(U, V) \sim (-30, -50)$ km/s and the inward-moving Horn feature at $(U, V) \sim (50, -20)$ km/s as, e.g., in fig. 22 of Gaia Collaboration et al. (2018b)—has therefore been classically explained by the *short fast bar’s* OLR.

The $(v_R, v_T) \sim (-U, V + v_{\text{circ}})$ velocity plane that we show in Figure 7(a) stacks all snapshots of our *Fiducial* test particle simulation for which the bar was oriented at an angle of 25 deg for stars located within 200 pc of $\mathbf{x}_{\odot} = (9 \text{ kpc}, 0, 0)$. This centers the survey volume on the OLR radius (see Table 1).

In velocity space, the orbit structure is more complicated than the simple ‘inside OLR \rightarrow anti-aligned $x_1(2)$ orbits \rightarrow outward-moving’. The ‘Hercules’-like OLR signature can contain also orbits from the $x_1(1)$: inward-moving parent orbits (Dehnen 2000) and highly librating orbits exhibiting outward-movements at the Sun (Fragkoudi et al. 2019).

The OLR in 4D phase-space.—The reason for the observed orbit overlap is the following: In the full 4D in-plane phase-space— (J_R, L_z) together with their canonical conjugate angle coordinates $(\theta_R, \theta_{\phi})$, or in the position-velocity space (\mathbf{x}, \mathbf{v}) —the two OLR orbit families are actually clearly distinct from each other. In 2D projection, it is only the angle space $(\theta_{\phi}, \theta_R)$ that reveals that the families do not overlap: $x_1(1)$ orbits have their apo- and pericenters at $\theta_{\phi} - \phi_{\text{bar}} = [0, \pm\pi]$ and $[\pm\pi/2]$, respectively; for the $x_1(2)$ orbits the opposite is true. In other 2D projections, the axisymmetric (L_z, J_R) , or velocity space as discussed above, or also in spatial positions, the two orbit families overlap in some regions. By adding a third dimension to action space, we can mitigate this.

The OLR in action- v_R space.—The same stars within 200 pc that were shown in velocity space in Figure 7(a), are in Figure 7(b) shown in the action plane, colour-coded by the relative number of outward (red) and inward (blue) moving stars. As expected from Figure 6, the OLR ARL also cleanly separates the red from the blue feature. (We colour-code action space by the stellar-number asymmetry in $\text{sign}(v_R)$ rather than $\langle v_R \rangle$ (as done in similar studies) to make the ‘red/blue’ feature visible down to $J_R \rightarrow 0$ where $\langle v_R \rangle \rightarrow 0$.)

To summarize, the OLR signature at the Solar azimuth consists in the local (Figure 7(b)) and extended (Figure 2) (L_z, J_R) action plane of:

- (i) a tendency between CR and OLR to be outward-moving/red,
- (ii) an outward-moving/red underdensity stripe to the low- L_z side of the ARL, and
- (iii) a sharp, inward-moving/blue, high- J_R scattering ridge to the high- L_z side of the ARL. The ridge is offset from the OLR ARL (e.g. Sellwood (2010); Hunt et al. (2019); see also Figure 2).

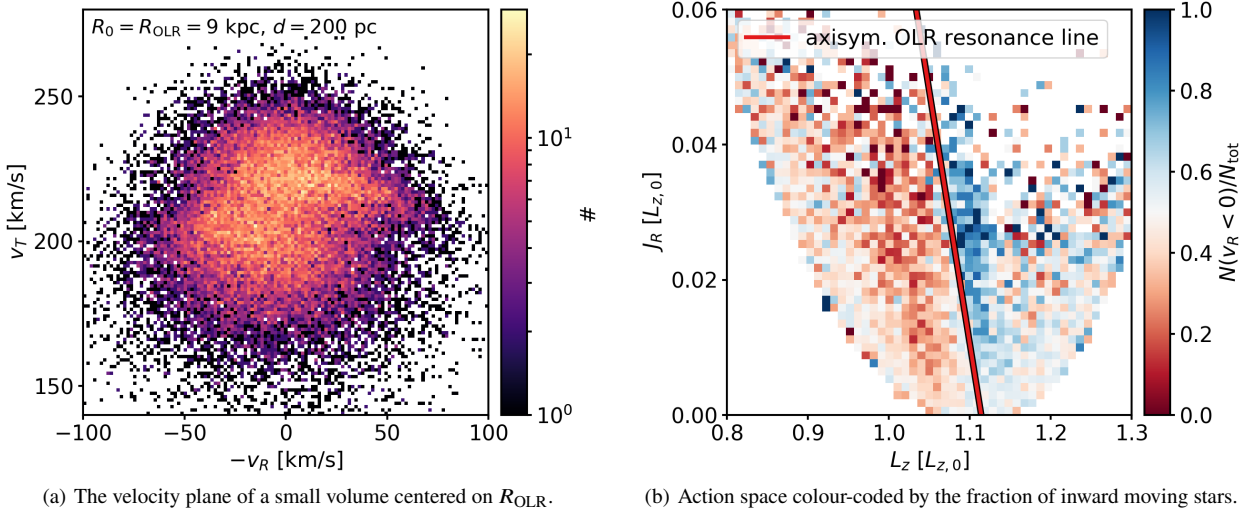


Figure 7. The outward/inward signature of the OLR in the Fiducial simulation. Panel 7(a) shows the classic velocity plane for a small volume ($d < 200$ pc) centered around $(R_{\text{OLR}}, \phi_{\text{bar}} - \phi, z) = (9 \text{ kpc}, 25 \text{ deg}, 0)$. Panel 7(b) shows the corresponding action plane (note the parabolic envelope due to the small volume), colour-coded by the fraction of inward-moving stars, analogous to Figures 1-2. Overplotted is the axisymmetric OLR ARL (with the “Hercules”-analogue at $v_T \lesssim 210$ km/s and the “Horn”-analogue at $(v_T, -v_R) \sim (220, 50)$ km/s), and in the action plane as a ‘red/blue’ feature cleanly separated by the OLR ARL.

This signature is well-studied in different coordinate spaces, where the features correspond...

... locally, in the velocity plane, to (i) an extended “Hercules”-like feature, (ii) an arch-shaped gap, (iii) a narrow “Horn”-like feature (Figure 7(a); see also, e.g., Dehnen 2000; Fux 2001; Fragkoudi et al. 2019).

... globally in the Galactic disk, as a function of Galactocentric (R, ϕ) , to a wide outward-/inward-moving wiggle in v_R at the same location as an underdensity/overdensity wiggle in stellar numbers (Figure C1(d); see also, e.g. Mühlbauer & Dehnen 2003; Hinkel et al. 2020).

... globally, in the (R, v_T) plane, to (i)-(ii) an outward-moving region and gap towards low R and v_T and (iii) the prominent, arch-like, inward-moving scattering ridge roughly near a line of constant $L_{z,\text{OLR}}$ (e.g., Fragkoudi et al. 2019, 2020; Hunt et al. 2019). J_R increases both towards higher and lower v_T , as well as towards smaller R across this ridge.

... globally, in the (L_z, ϕ) plane, to thinner parallel (ii) red/underdense and (iii) blue/overdense stripes at constant L_z (Figure A1 in Appendix A; see also, e.g., Monari et al. 2019b; Chiba et al. 2019).

5 RESULTS

5.1 Measuring the bar’s pattern speed using the outward/inward feature of the OLR

The outward/inward velocity flip created by the bar’s OLR has often been used to identify the location of this resonance. Comparing Figure 7(b) (< 200 pc) with Figure 2 (< 4 kpc), shows that action space conserves the alignment of the OLR’s outward/inward feature around the ARL when going from the local to the extended Solar neighbourhood. The *Gaia* data allow therefore to search for the OLR beyond the local velocities. The actions in particular enable us for the first time to show all OLR candidates in one, clean overview plot in Figure 8.

Every pair of outward/inward moving stripes separated by a

line of the same slope as an ARL is a candidate for the signature of the bar OLR. Each OLR candidate corresponds to a specific Ω_{bar} . In the *Gaia* DR2 RVS actions, we count three prominent ‘red/blue’ features (see Figures 1 and fig. 7 in T19). A decrease in Ω_{bar} shifts the OLR ARL toward larger L_z and makes it steeper. We read off the value for Ω_{bar} whenever the OLR ARL separates a red stripe on the left from a blue stripe on the right, as illustrated in Figure 8. These three direct Ω_{bar} measurements assume the MWPotential12014 potential model, and are $\Omega_{\text{bar}} \sim 1.85 \Omega_0$, $\Omega_{\text{bar}} \sim 1.27 \Omega_0$, and $\Omega_{\text{bar}} \sim 1.63 \Omega_0$.

We also implemented the more recent MW potential model by Eilers et al. (2019) (with $R_0 \equiv 8.122$ kpc, $v_0 \equiv 229.8$ km/s, $L_{z,0} \sim 1866$ kpc km/s, and $\Omega_0 \sim 28.3$ km/s/kpc in our implementation), recalculated actions and frequencies, and applied the same strategy to measure pattern speeds at these OLR candidates of $\Omega_{\text{bar}} \sim 1.85 \Omega_0$, $\Omega_{\text{bar}} \sim 1.27 \Omega_0$, and $\Omega_{\text{bar}} \sim 1.70 \Omega_0$, respectively.

Only one of these three candidates can be the bar’s true OLR and pattern speed. We summarize all measurements in Table 1.

The Hercules pattern speed $1.85 \Omega_0$ is derived from the strongest ‘red/blue’ feature in the data, the transition from the Hercules to the Horn moving groups (see T19 for the location of the moving groups in action space). Both potentials give the same result in units of Ω_0 , owing to this assumed OLR being close to $L_z/L_{z,0} = 1$. With the fixed assumption for the Schönrich et al. (2010) Solar motion, the measurement of this $\Omega_{\text{bar}}/\Omega_0$ is therefore only weakly dependent on the shape of the rotation curve and quite robust.

The Hat pattern speed $1.27 \Omega_0$ is derived from the second strongest ‘red/blue’ feature in the *Gaia* DR2 action space which is located at high J_R around $L_z/L_{z,0} \sim 1.3$ and continues—albeit much weaker—down to $J_R = 0$. This feature projects to the Hat moving group in the local velocities (at $V \sim 40$ km/s in Gaia Collaboration et al. 2018b). The measurements for the two potentials differ by almost $0.1 \Omega_0$, indicating that for this pattern speed, derived from an OLR candidate further away from the Sun, the shape of the rotation curve does matter.

The Sirius pattern speed $1.63 \Omega_0$ is derived from a third

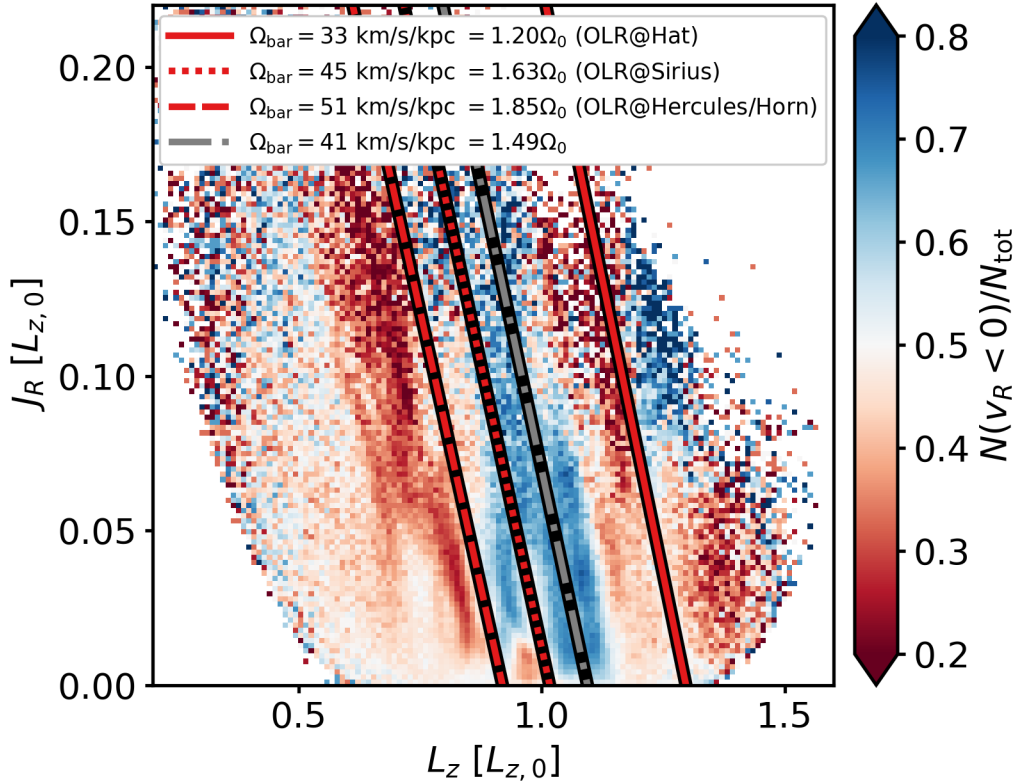


Figure 8. All candidates for the characteristic outward/inward (‘red/blue’) signature of the MW’s bar OLR within 3 kpc from the Sun in *Gaia* DR2 RVS. We show the v_R -asymmetry as a function of the axisymmetric actions estimated in the MWPotential12014 ($\Omega_0 = 27.5$ km/s/kpc). The *Gaia* action space reveals three prominent ‘red/blue’ features at slopes similar to that of ARLs. We position (the red) OLR lines such that each separates an outward- from an inward-moving stripe, as observed in the simulation (see Figure 7). These OLR locations correspond to specific pattern speeds, thus allowing us to read off possible pattern speeds for the bar directly from the data. The corresponding pattern speeds, as well as the moving groups of the local Solar neighbourhood that could be related to this OLR, are indicated in the legend. In addition, we overplot (in grey) the OLR line for a pattern speed of $1.49\Omega_0 = 41$ km/s/kpc (Sanders et al. 2019; Bovy et al. 2019), which does not separate a red from a blue feature (see also Figure 12 and Section 6.3).

‘red/blue’ feature, in the *Gaia* action data close to $J_R \sim 0$ and $L_z/L_{z,0} \sim 1$. In the projection to local velocity space, this corresponds to the transition from the outward-moving Hyades to the inward-moving Sirius group. This OLR candidate feature continues above the Horn, around the ARL at $J_R \sim 0.1L_{z,0}$. In Section 6.1, we discuss these pattern speeds in detail and compare to the literature in Section 6.3.

5.2 The imprint in the vertical action due to the OLR

$\langle J_z \rangle$ gradient around the OLR.—In the *Gaia* data, the ridges in (L_z, J_R) are related to signatures in mean vertical action J_z (Figure 1). In Section 3.2, we found that our test particle simulations exhibit signatures in mean J_z around the OLR and 1:1 resonance (Figures 2 and 11). This becomes especially obvious in Figures 9(a) and 9(b), where we show number counts and average J_z for the Fiducial model as a function of L_z only.

The epicyclic approximation for near-circular disk orbits assumes that vertical and radial motions are decoupled. The in-plane bar resonance should therefore not change the J_z of individual disc stars. And indeed, in the Fiducial model, the average relative change in J_z is only 0.6 percent, as compared to 70 percent in J_R (where $\sigma_R > \sigma_z$). The observed J_z -signature at the OLR therefore has to be a cumulative effect in the stellar distribution induced by the bar.

Figure 10(a) shows again the \mathbf{J}_{mean} distribution from Figure 5, but colour-coded by the stars’ J_z . We find that the exact \mathbf{J}_{mean} location at all the resonances shifts with the value of J_z : The resonances appear to sort stars according to their J_z .

This sorting is the consequence of the combination of two different properties:

- (i) In axisymmetric Galaxy potentials the ARL depends on J_z .
- (ii) In a barred Galaxy potential, a resonant star oscillates around the ARL with the same J_z .

The J_z -dependence of the ARL.—Property (i) follows from the in-plane orbital frequencies being dependent on J_z in galaxy-like potentials—also in the case of axisymmetry. In Figure 10(b), we show the OLR ARL not only for $J_z = 0$ as usual, but also for different $J_z > 0$. The lines shift towards smaller (L_z, J_R) with increasing J_z . The dependence of $\Omega_{i,\text{axi}}$ on (L_z, J_R, J_z) depends on the exact form of the (axisymmetric) galaxy potential. A general, analytic derivation of this property is non-trivial and beyond the scope of this work. Numerical experiments can however provide some intuition. In an axisymmetric potential, the circular and epicycle frequencies

$$\Omega(R_g | \Phi_{\text{axi}}) \equiv \left(\frac{1}{R} \frac{\partial \Phi_{\text{axi}}}{\partial R} \right)_{(R=R_g, z=0)}^{1/2}, \quad (11)$$

$$\kappa(R_g | \Phi_{\text{axi}}) \equiv \left(\frac{\partial^2 \Phi_{\text{axi}}}{\partial R^2} + \frac{3}{R} \frac{\partial \Phi_{\text{axi}}}{\partial R} \right)_{(R=R_g, z=0)}^{1/2} \quad (12)$$

| Pattern speed model name | Pattern speed | | | OLR radius R_{OLR} [kpc] | Bar length | | Bar strength $\alpha_{m=2}$ | Notes |
|--------------------------|--|-------------------------------------|---|---|---------------------------|--------------------------------|--------------------------------|---|
| | derived from OLR-like signature at | Ω_{bar} [km/s/kpc] | Ω_{bar} [Ω_0] | | R_{bar} [kpc] | $R_{\text{CR}}/R_{\text{bar}}$ | | |
| Fiducial | - | 40 | 1.45 | 9.0 | 4.5 | 1.25 | 0.01 | used only in the generic investigation of the bar's effect on the axisym. action space in Sections 3-5 |
| Hercules | outward Hercules/ inward Horn, $L_z \sim 0.9L_{z,0}$ | 51 52 [†] | 1.85 1.85 [†] | 7.3 7.5 [†] | 3.5 | 1.26 | 0.01 | c.f. <i>short fast bar</i> in Dehnen (2000), Antoja et al. (2014) |
| Sirius | outward Hyades/ inward Sirius, $L_z \sim 1.0L_{z,0}$ | 45 48 [†] | 1.63 1.70 [†] | 8.2 8.1 [†] | 4 | 1.26 | 0.015 | - |
| Hat | outward/inward at the Hat, $L_z \sim 1.3L_{z,0}$ | 33 36 [†] | 1.20 1.27 [†] | 10.7 10.5 [†] | 5 | 1.35 | 0.015 | c.f. <i>long slow bar</i> in Pérez-Villegas et al. (2017), Monari et al. (2019a) |
| S19B19 | - | 41 ± 3 | 1.49 ± 0.1 1.45 ± 0.1 [†] | 8.8 ± 0.6 9.3 ± 0.7 [†] | - | - | - | <i>slightly faster slow bar</i> with pattern speed taken from Sanders et al. (2019), Bovy et al. (2019). Hercules/Horn related to the 1:4 OLR (Hunt & Bovy 2018). |

Table 1. Overview of the bar pattern speeds considered in this work. The pattern speeds of the Hercules, Hat, and Sirius bar models were derived from the *Gaia* DR2 data (see text for details) for the MWPotential12014 (Bovy 2015, with $\Omega_0 = 27.5$ km/s/kpc). We have run test particle simulations for these pattern speeds and have assumed a bar orientation of $\phi_{\text{bar}} = 25$ deg with respect to the Solar azimuth for a pure quadrupole bar model. The bar length was chosen to satisfy $R_{\text{CR}}/R_{\text{bar}} \sim 1.2$ (Contopoulos 1980; Athanassoula 1992) and the bar strengths $\alpha_{m=2}$ (see Appendix C2) were chosen to create OLR signatures of roughly similar strength. The pattern speeds marked with [†] were derived analogously from the *Gaia* DR2 data, but for actions and frequencies estimated in the MW potential by Eilers et al. (2019) with $\Omega_0 = 28.3$ km/s/kpc. The S19B19 pattern speed is included as a comparison with another bar model in the literature.

(from eq. (3.79) in Binney & Tremaine 2008) can be considered as a property of the potential. For a near-circular orbit in the epicycle approximation, these frequencies evaluated at its R_g are the real orbital frequencies. It can be shown that for an orbit with $J_R \gg 0$ and $J_z \gg 0$ integrated in an axisymmetric potential these Ω and κ are closer to the real⁹ orbital frequencies Ω_R and Ω_ϕ when evaluated at the time-averaged radial coordinate $\langle R(t) \rangle_t$ of the orbit rather than at R_g . Only in the limit $J_R \rightarrow 0, J_z \rightarrow 0$ also $\langle R(t) \rangle_t \rightarrow R_g$. In general, an orbit has a larger $\langle R(t) \rangle_t$ if any of the three actions (J_R, L_z, J_z) is larger. We therefore expect anti-correlations between the actions with the frequencies that satisfy the resonance condition. We observed the J_z -dependence of the ARL also for the Stäckel potential KKS-Pot previously used in Trick et al. (2017). So even in separable potentials—where the momentum $p_i(x_i)$ is a function of x_i only (with the prolate confocal coordinates $x_i \in [\lambda, \nu, \phi]$) and the actions are $J_i \propto \int_{x_{i,\min}}^{x_{i,\max}} p_i(x_i) dx_i$ —the frequencies $\Omega_{i,\text{axi}}(\mathbf{J}) = \partial \mathcal{H}_{\text{axi}}(\mathbf{J}) / \partial J_i$ are not independent of $J_z \equiv J_\nu$.

Property (ii) is illustrated in Figure 10(b), where we show in addition the oscillation midpoints for the true resonant OLR stars, demonstrating that the stars oscillate around (or at least close to) their actual, J_z -dependent ARL, causing therefore the gradual “sorting” of the stars by J_z at the resonance.

The J_z -sorting is best visible at the OLR.—Figure 10(c) shows that the oscillation amplitudes of resonant OLR and CR stars are independent of J_z . The sorting by J_z of the oscillation midpoints (Figure 10(a)) remains therefore also visible in the phase-mixed

distribution (Figure 9(b)). The same (m, l) -dependence of resonant scattering and oscillation that creates the high- J_R OLR ridge also makes the J_z signature better visible for the OLR than at CR: At the OLR (and also the 1:1 resonance), the asymmetric scattering towards higher J_R and L_z creates a sharply defined ridge dominated by resonant, J_z -sorted stars. At CR, the weak J_R - and symmetric L_z -scattering as well as strong L_z -oscillation mixes the resonant with non-resonant stars, diluting the J_z signature.

Context to other studies.—The Galactic disc’s orbit pattern in $\langle J_z \rangle$ as a function of the (L_z, J_R) plane found by T19 is related to the vertical wave-like signatures in projections of (\mathbf{x}, \mathbf{v}) : in $\langle v_z \rangle$ vs. R_g (Schönrich & Dehnen 2018), $\langle v_z \rangle$ vs. (R, v_T) (Laporte et al. 2019), $\langle z \rangle$ and $\langle |z| \rangle$ vs. (R, v_T) (Khanna et al. 2019). This pattern in the vertical motion is aligned with the overdensities and v_R -undulations (Laporte et al. 2019; Friske & Schönrich 2019; Khanna et al. 2019). As a cause for this observed coupling of radial and vertical motions, several authors suggested interactions of a satellite galaxy like the Sagittarius dwarf with the Galactic disc (Schönrich & Dehnen 2018; Carrillo et al. 2019; Khanna et al. 2019).

In the absence of satellite interactions, secular resonance phenomena can also create correlations between radial and vertical motions. Binney (1981), for example, showed that coupling between the in-plane and vertical orbital frequencies can excite large vertical motions via instabilities. Masset & Tagger (1997) showed that a spiral wave can, at its OLR, transfer energy to warp waves in the Galactic disk. The J_z -sorting mechanism at the OLR presented in this work is different as it leaves the J_z of the orbits unchanged, and neither instabilities nor warps with $\langle z \rangle \neq 0$ occur.

In our simulation, the $\langle J_z \rangle$ vs. (L_z, J_R) signature caused by bar resonances translates into wiggles in the average absolute values of the vertical velocity, $\langle |v_z| \rangle$ vs. L_z . This is because a higher J_z describes an orbit that reaches higher above/below the disk and

⁹ We have explicitly checked in our simulation that for orbits integrated in the axisymmetric potential, the action frequencies agree with the real frequencies derived from a Fourier-analysis of the orbit, i.e., $\Omega_{\phi,\text{axi}} \equiv \partial \mathcal{H}_{\text{axi}} / \partial J_\phi = \Omega_{\phi,\text{true}}$ and $\Omega_{R,\text{axi}} \equiv \partial \mathcal{H}_{\text{axi}} / \partial J_R = \Omega_{R,\text{true}}$.

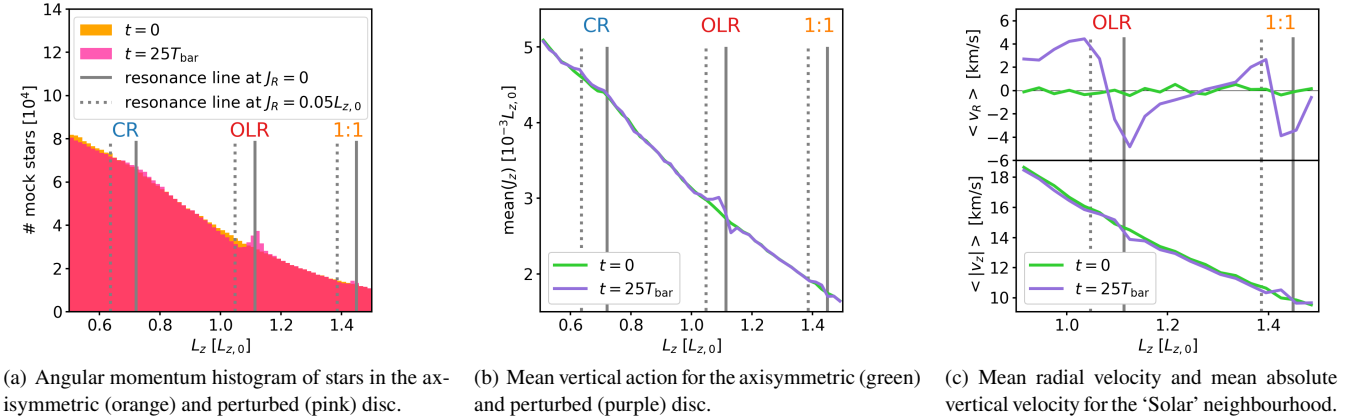


Figure 9. The vertical action signatures as a function of L_z only. All panels show the resonance signature in the Fiducial bar simulation (at $t = 25T_{\text{bar}}$ within $|z| < 500$ pc) in star counts (Panel 9(a)) and mean vertical action $\langle J_z \rangle$ (Panel 9(b)), comparing them to the axisymmetric disc at $t = 0$. The grey vertical lines denote $L_z(J_R | \text{ARL})$ evaluated at $J_R = (0, 0.05)L_{z,0}$ for CR, OLR, and the 1:1 resonance. Panel 9(c) shows the mean radial and absolute vertical velocities, $\langle v_R \rangle$ and $\langle |v_z| \rangle$ (for the 'Solar' neighbourhood, $R_\odot = 8$ kpc, $d < 4$ kpc), demonstrating that bar resonances could contribute to coupled radial and vertical velocity waves in the Galactic disc. (Note that for this effect still $\langle v_z \rangle = \langle z \rangle = 0$.)

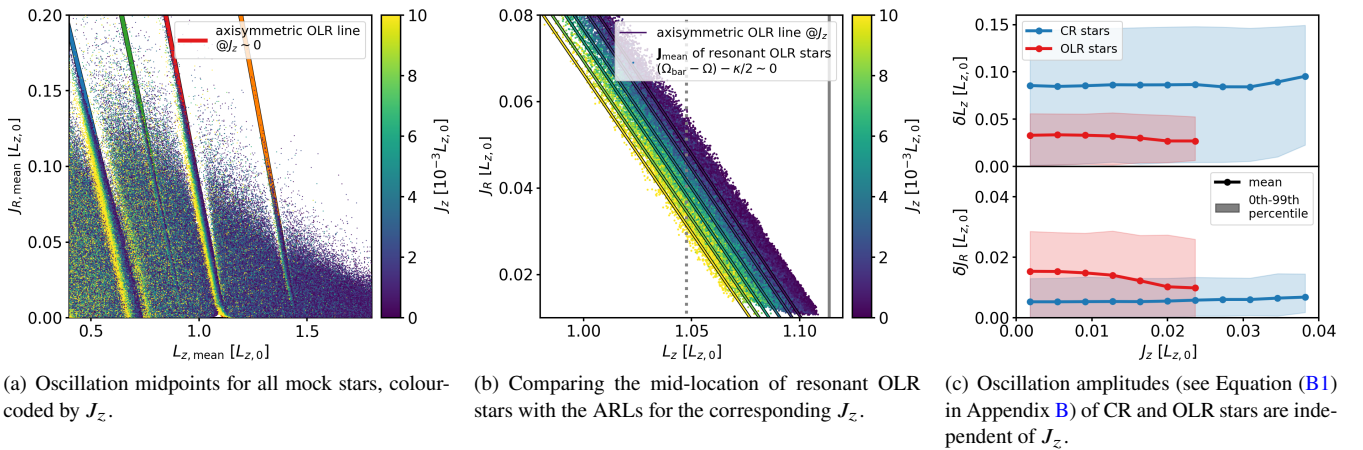


Figure 10. The underlying reason for the vertical action J_z feature at the resonances in the Fiducial simulation shown in Figures 2 and 9 is (i) that the ARL's location depends on J_z (lines in Panel 10(b)), and (ii) the real resonant stars have their orbit midpoints close to the ARL with the same J_z (points in Panel 10(b)). This leads to the J_z -sorting of (the orbit midpoints of) stars at all resonances (Panel 10(a)). The J_z -independence of the oscillation around the ARLs (Panel 10(c)) conserves the J_z ordering during oscillation.

has therefore higher values of v_z when crossing the Galactic plane. As the same amount of stars is moving upwards- and downwards, $\langle v_z \rangle = \langle z \rangle = 0$, but $\langle |v_z| \rangle$ can still be larger. At the OLR, the $\langle |v_z| \rangle$ vs. L_z signature is therefore naturally coupled with the OLRs $\langle v_R \rangle$ wiggle, as shown in Figure 9(c). Even though the resonances do not affect $\langle v_z \rangle \sim 0$, and the difference in $\langle |v_z| \rangle$ with respect to the axisymmetric disc is no larger than ~ 1 km/s, our work suggests a novel mechanism how in-plane bar resonances *could contribute* to the observed correlation between radial and vertical motions.

6 DISCUSSION

6.1 Comparison between the *Gaia* data and the test particle simulation

The main result of this work is the derivation of three bar OLR and pattern speed candidates from the local *Gaia* DR2 action data in

Figure 8. In the following, we discuss these pattern speeds in Figure 11 by (i) investigating the location of the CR, 1:4, and 1:1 resonance lines in addition to the OLR in the *Gaia* data, and (ii) by comparison to test particle simulations for these pattern speeds (see Table 1 for the model parameters).

The following criteria need to be fulfilled for the pattern speed to be a realistic candidate:

[OLR red/blue]—The OLR at the Solar azimuth has to exhibit an outward/inward feature around the OLR resonance line (see Section 4.6). For our three derived pattern speeds, this is fulfilled by construction. (3rd column in Figure 11.)

[OLR ridge]—An underdensity region vs. overdensity ridge in the *Gaia* data associated with this OLR is expected (see Section 4.2). Our simulation is neither self-consistent nor does it have a cosmological context or spiral arms. Fragkoudi et al. (2019, 2020) showed, however, that even in these more realistic cases the OLR ridge is prominent. Moreover,

the ridge should have a similar slope in action space as in the simulation. In the discussion, we use the nomenclature for the ridges in the *Gaia* data from T19. (2nd column in Figure 11.)

[OLR Jz]—We expect a gradient in $\langle J_z \rangle$ with L_z across the OLR resonance (see Section 5.2). (4th column in Figure 11.)

[1:1]—Based on the simulations in Figure 11, we expect an outward/inward feature, a scattering ridge, and a J_z signature at the 1:1 resonance. (Resonant orbits at the 1:1 bar resonance have been studied by, e.g., Dehnen (2000), Athanassoula et al. (1983), and Contopoulos & Grosbol (1989).)

[1:4]—The 1:4 resonance of a bar with non-zero $m = 4$ component might create an overdensity ridge and induce outward/inward features, as suggested by Hunt & Bovy (2018), Hunt et al. (2019), and Monari et al. (2019a). In this work, we have not included an $m = 4$ Fourier component into the bar model to simplify the discussion, even though we have run corresponding simulations (with integration times of more than 20 bar periods). For bar strengths of the order of $|\alpha_{m=4}| \sim 0.0005$ no significant 1:4 signatures were observed: Overdensity ridges developed only in the case of large 1:4 scattering in simulations with very strong $|\alpha_{m=4}| \gtrsim 0.001$; v_R -asymmetry features did not develop at all as in our simulations only one class of 1:4 orbits got populated by stars—which one depended on the alignment of the $m = 2$ and the $m = 4$ components with respect to each other. This is in contrast to the above mentioned studies (with backwards orbit integration times for a maximum of 10 bar periods), in which, as Hunt et al. (2019) demonstrated, two classes of 1:4 orbits are populated, creating ‘red/blue’ features analogously to the OLR in the case of boxy bars ($\alpha_{m=4} < 0$), and analogously, ‘blue/red’ features in the case of pointy bars with ansae ($\alpha_{m=4} > 0$). Fux (2001, see their fig. 4) discussed that of the two classes of 1:4 orbits one is stable and the other one is unstable. This could explain the difference to our simulations. Real galaxies might, however, slowly repopulate the unstable 1:4 orbits as more stars get perturbed into the appropriate trapping regions of phase-space by non-axisymmetric structure beyond the bar. Overall, the expected signatures at the 1:4 resonance depend on the strength and orientation of the $m = 4$ bar component, and the evolution history how different orbits got populated. As neither of this is well constrained in the MW, we treat the 1:4 resonance only as a weak criterion on the pattern speed for now.

6.1.1 The Hercules pattern speed

The first two rows in Figure 11 show that the Hercules pattern speed satisfies the [OLR red/blue], [OLR ridge], [OLR Jz] and [1:1] criteria.

Agreement.—Around the OLR in action- v_R space, data and simulation are strikingly similar. Because the OLR is closer to the bar, the OLR signature is stronger than in the Fiducial simulation. Because the radial velocity dispersion is higher closer to the Galactic center, the underdensity/overdensity and outward/inward OLR signatures are further apart, as demonstrated by Mühlbauer & Dehnen (2003, see their figs. 3 and 4). The OLR ridge of this proposed model is the action space ridge D1/blue related to the

Horn. It even has a similar slope in the test particle simulation. The $\langle J_z \rangle$ data show J_z trends across the OLR. The 1:1 resonance is located in *Gaia*’s action space around $L_z \sim 1.2L_{z,0}$, next to the weak H/gold ridge. We show in Figure 11 for the region marked by a black box the v_R -asymmetry for stars within $d < 600$ pc as an insert. Locally, a weak and narrow ‘red/blue’ feature separated by the 1:1 resonance line is observed, as predicted in the simulation.

Open questions.—The [1:4] resonance line falls together with a blue/red transition in the *Gaia* data. It is unclear if this supports or contradicts the Hercules model. The D1/blue ridge is not the strongest ridge in the *Gaia* data, contrary to what is expected. Can a different bar strength or bar evolution explain this difference? Or do spiral arms create stronger ridges than the bar? Why is the 1:1 signature so weak and only locally visible?

Conclusion.—The action data exhibits just enough agreement with the model prediction to not yet rule-out the Hercules bar pattern speed model. The substructure present in the Hercules region of the *Gaia* data suggests that more than one mechanism might be at work in this region.

6.1.2 The Hat pattern speed

The last two rows in Figure 11 show that the Hat pattern speed satisfies the [OLR red/blue], [OLR ridge], [OLR Jz] and [1:4] criteria.

Agreement.—The prominent ‘blue’ ridge of this proposed OLR feature is called I/yellow in T19 and projects to the Hat. The corresponding ‘red’ region is the most prominent underdensity of the *Gaia* DR2 action space. In this model, the 1:4 resonance falls together with the Sirius moving group: If the 1:4 resonance indeed creates an inward-moving ridge, G1/orange or F1/red are good candidates.

Open questions.—The 1:1 resonance does not fall within *Gaia*’s survey volume; would it support the Hat pattern speed?

Conclusion.—Overall, the Hat pattern speed agrees with the model prediction.

6.1.3 The Sirius pattern speed

The 3rd and 4th row in Figure 11 show that the Sirius pattern speed might satisfy the [OLR red/blue], [OLR ridge], [OLR Jz], [1:1], and [1:4] criteria.

Agreement.— This pattern speed positions *two* ARLs—the OLR and the 1:1 resonance—roughly between ‘red/blue’ features. The two strongest ridges in the *Gaia* data (Sirius F1/red and G1/orange and the Hat I/yellow) are at the same location as in the simulation with clear J_z trends. The 1:4 ARL falls into the outward-moving Hercules region, as in our simulation.

Open questions.—The ‘red’ part of this OLR candidate in the *Gaia* data—which is supposed to reach from low to high J_R —is partly obscured by the Horn; the ‘blue’ part exhibits a wide double-peaked structure; which mechanisms could explain this? For the 1:1 resonance, the correct ‘red/blue’ flip shows up only for $J_R \gtrsim 0.1L_{z,0}$ as the slope of the 1:1 ARL differs from the slope of the ‘red/blue’ feature in the *Gaia* data; this alignment works even less well in the Eilers et al. (2019) potential; could this be resolved with a different potential model?

Conclusion.—While being overall the weakest candidate, it is in any case noteworthy that the $m = 2$ component of a bar is able to explain *two* ridges and ‘red/blue’ features.

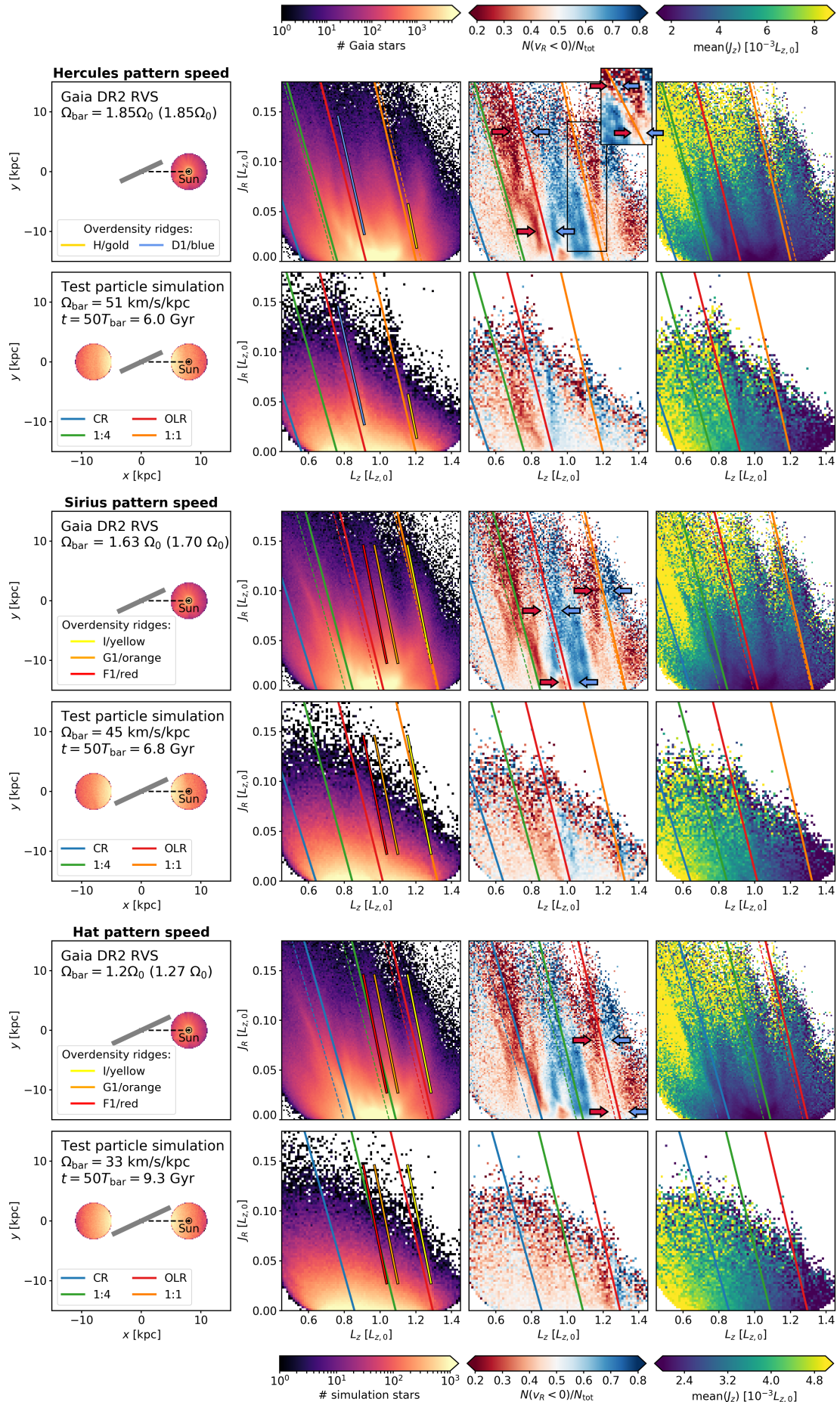


Figure 11. (Figure caption on the next page.)

Figure 11 – *continued* Location of the bar’s ARLs in the *Gaia* DR2 RVS action data (upper panels; c.f. Figure 1) and comparison with a bar-only test particle simulation (lower panels) for the three pattern speeds determined in Figure 8 based on the *MWPotential2014*. Ω_{bar} is given in units of $\Omega_0 = 27.5$ km/s/kpc and km/s/kpc in the first column. The dashed lines correspond to the ARLs when assuming the *Eilers et al. (2019)* potential, with the corresponding Ω_{bar} mentioned in brackets in units of $\Omega_0 = 28.3$ km/s/kpc. All simulation parameters are summarized in Table 1. The top colourbar refers to the *Gaia* data, the bottom colourbar to the simulation data. The solid lines with black borders denote the high- J_R overdensity features identified in T19 which could correspond to the OLR and 1:1 scattering ridges visible in the test particle simulation, and the 1:4 ridge expected for strong $m = 4$ bar components (c.f. *Hunt & Bovy 2018; Hunt et al. 2019; Monari et al. 2019a*). For the *Hercules* bar pattern speed in the *Gaia* data in the first row, we show an insert for stars within $d < 600$ pc only.

6.2 Caveats

The only strong assumptions in our ARL-positioning method to measure the pattern speed that we introduced in Section 5.1 are that (a) the spiral arms are weak enough to not wash out the OLR’s ‘red/blue’ feature, (b) the MW’s bar pattern speed is constant, (c) the axisymmetric potential model, and (d) the assumed Solar motion.

The ILR of a transient spiral mode can cause an outward/inward signature aligned with the ARL very similar to the OLR of the bar, as presented in fig. 7 by *Sellwood et al. (2019)*. *Hunt et al. (2019)* showed that transient winding spiral arms (that are co-rotating everywhere) can cause a time-dependent pattern of inward and outward moving features. Simulations by *Fujii et al. (2019)* and *Hunt et al. (2019)* noted that the bar OLR signature can get washed out in some time steps or with some spiral arm models. As we don’t know much about the nature and strength of the spiral arms in the Solar vicinity yet, nothing can be done about assumption (a).

Chiba et al. (2019) investigated the effect of a slowing bar, whose resonances sweep outward in the disk with time. A slowly decelerating bar widens the ‘blue’ part of the OLR signature (their fig. 18). A rapidly decelerating bar slightly shifts the location of the OLR’s scattering ridge and ‘red/blue’ feature with respect to the ARL (their fig. 19). As the true deceleration rate of the bar is not known, we cannot estimate how much assumption (b) biases the ARL-positioning method.

The influence of assumption (c) was tested by calculating actions and frequencies also in different potential models. For changes in $v_{\text{circ}}(R_0)$ of up to 20 km/s, and in R_0 up to 0.3 kpc, as well as experimenting with the slope of the rotation curve, we found deviations from the measured values for Ω_{bar} in Table 1 of up to but no more than $0.1 \Omega_0$, which pushes the pattern speed by ~ 3 km/s/kpc. As an explicit test, we stated the pattern speeds derived using the *Eilers et al. (2019)* potential both in Figure 11 and Table 1.

Another source of error is the uncertainty in our knowledge of the Solar motion, assumption (d), which can also shift the distribution across the action plane and therefore Ω_{bar} . In this work we used $(U_{\odot}, V_{\odot}, W_{\odot}) = (11.1, 12.24, 7.25)$ km/s as measured by *Schönrich et al. (2010)*. We leave this error source unexplored for now, given the already significant uncertainty of $0.1\Omega_0$ due to the assumed potential model.

6.3 Comparison to the literature

6.3.1 The short fast bar model

Our *Hercules* pattern speed $\Omega_{\text{bar}} = 51$ km/s/kpc $= 1.85\Omega_0$ re-derived from action space the classic *short fast bar* model. Previous pattern speed measurements based on the *Hercules/Horn* bimodality include $\Omega_{\text{bar}} = 1.85 \pm 0.15\Omega_0$ by *Dehnen (2000)*, and $\Omega_{\text{bar}} = 1.81 \pm 0.02\Omega_0$ for $\phi_{\text{bar}} = 25$ deg by *Antoja et al. (2014)*. From modeling the effect of the bar on the Oort constants, *Minchev et al. (2007)* found a pattern speed of $\Omega_{\text{bar}} = 1.87 \pm 0.04\Omega_0$. This corresponds to a CR radius of 4.3 – 4.4 kpc in our two potential models. Independent, older measurements also suggested CR radii in the range $R_{\text{CR}} \in$

[3.0 – 4.5] kpc from gas dynamics (*Englmaier & Gerhard 1999; Fux 1999; Bissantz et al. 2003*).

Substructure in the *Gaia* action-angle data beyond the resonances of a *short fast bar*—in particular the ridges associated with *Sirius*—could be reproduced by a transient winding spiral, as shown by *Hunt et al. (2019)* (their model H).

We also found weak evidence for the corresponding 1:1 resonance in action space. For local stars with $d < 200$ pc, this was first mentioned by *Dehnen (2000)*: the velocity space above *Sirius* could look like the 1:1 resonance of a fast bar. We noted, however, that this ‘red/blue’ signature is, however, only visible out to $d \sim 600$ kpc.

6.3.2 The long slow bar model

Our *Hat* pattern speed $\Omega_{\text{bar}} = 33 - 36$ km/s/kpc $= 1.20 - 1.27\Omega_0$ is quite close to (albeit slower than) some pre-*Gaia* DR2 measurements from the Galactic center known as the *long slow bar* model: *Li et al. (2016)* measured $\Omega_{\text{bar}} = 1.3\Omega_0$ (for $\Omega_0 = 210/8.3$ km/s/kpc) from comparing the gas flow in the MW (HI and CO (l, v)-diagrams) to N -body simulations. *Portail et al. (2017)* found $\Omega_{\text{bar}} = 1.34 \pm 0.12\Omega_0$ (for $\Omega_0 = 238/8.2$ km/s/kpc) from made-to-measure modeling of the bar (3D red clump star density (*Wegg & Gerhard 2013*) and kinematics from the BRAVA survey (*Kunder et al. 2012*) and others). A more recent study by *Clarke et al. (2019)* found that *Gaia* DR2 and VIRAC (*Smith et al. 2018*) proper motions of giant stars in the Galactic bar region are consistent with $\Omega_{\text{bar}} \sim 1.32\Omega_0$ (for $\Omega_0 = 233/8.2$ km/s/kpc).

The CR of the *long slow bar* might explain the *Hercules* stream (*Pérez-Villegas et al. 2017*). This was supported by *Binney (2020b)* using action-based torus modeling of the *Hercules* stream in *Gaia* DR2, finding $\Omega_{\text{bar}} = 1.14 - 1.25\Omega_0$ (for $\Omega_0 = 239/8.27$ km/s/kpc). The *Gaia* DR2 action data and the *Hat*’s ‘red/blue’ feature in this work provide an independent constraint on this pattern speed for the slow *Hat* bar.

Fragkoudi et al. (2019, 2020) showed, however, that CR does not give rise to a *Hercules/Horn* bimodality and concluded that this strong observed bimodality cannot be a consequence of CR alone in a slow bar scenario, but requires the existence of an additional perturbation mechanism.

Model F in *Hunt et al. (2019)* demonstrated that winding spiral arms could be responsible for differences between the *long slow Hat* bar model and the *Gaia* data.

Our pure-quadrupole bar model does not include an $m = 4$ component. Some recent studies—which were developed independently and in parallel to this work—did consider the effect of higher-order bar components: small but notable discrepancy of other local-only pattern speed measurements from bar resonances—our ‘OLR = *Hat*’ and the ‘CR = *Hercules*’ by *Binney (2020b)*—of $\Omega_{\text{bar}} \sim 1.2\Omega_0$ with respect to Galactic center measurements of $\sim 1.32\Omega_0$.

6.3.3 An intermediate bar

Kalnajs (1991) had first pointed out that the outward-moving *Hyades*

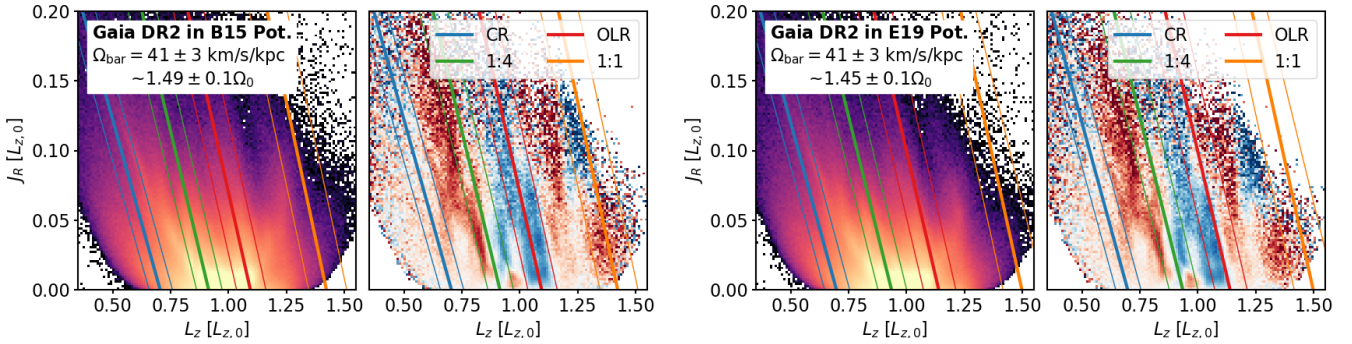


Figure 12. The *Gaia* DR2 RVS action data, overplotted with the ARLs for a pattern speed of 41 ± 3 km/s/kpc (corresponding to $1.49 \pm 0.1\Omega_0$ for the *MWPotential2014* by Bovy (2015), left panels; $1.45 \pm 0.1\Omega_0$ for the Eilers et al. (2019) potential, which has recently been measured from data in the inner Galaxy (Sanders et al. 2019; Bovy et al. 2019; S19B19 hereafter). (The thin lines correspond to $\Omega_{\text{bar}} \pm 0.1\Omega_0$.) For this pattern speed, the 1:4 resonance line (green) separates the prominent ‘red/blue’ feature close to Hercules. Hunt & Bovy (2018) proposed that a bar with a similar pattern speed and a strong $m = 4$ Fourier component could be responsible for the Hercules stream. The OLR line (red) for this *slightly faster slow* S19B19 bar pattern speed does, however, not separate a prominent outward from an inward-moving (‘red/blue’) feature as we would expect.

and the inward-moving Sirius streams could form together the signature of the bar’s OLR. In this work, we showed that this ‘red/blue’ OLR candidate is not just visible in the classical local moving groups at $J_R \lesssim 0.02L_{z,0}$, but continues at $J_R \gtrsim 0.05L_{z,0}$ and out to ~ 3 kpc from the Sun. That the corresponding Sirius pattern speed $\Omega_{\text{bar}} \sim 1.63 - 1.70\Omega_0$ (as measured in this work) has not attracted more attention in the literature is most likely because it cannot provide an explanation for the Hercules/Horn. However and interestingly, the recent study by Hunt et al. (2019) found that a bar pattern speed of $1.55 - 1.65\Omega_0$ together with a $m = 4$ bar component and a transient winding spiral arm (their Figure 9; Model G) looks quite similar to the *Gaia* data, with the combination of the bar 1:4 resonance and the winding spiral causing the substructure in the Hercules region.

6.3.4 The slightly faster slow bar

Recent studies modelled the central bar region using versions of the Tremaine & Weinberg (1984) method. They converge on pattern speeds around $\Omega_{\text{bar}} \sim 40$ km/s/kpc. Sanders et al. (2019) and Bovy et al. (2019) both quote $\Omega_{\text{bar}} = 41 \pm 3$ km/s/kpc. Sanders et al. (2019) modelled the transverse proper motions of red giants from *Gaia* DR2 and the VVV survey (Smith et al. 2018) observed towards the Galactic center. Independently, Clarke et al. (2019) found that this data agrees with models for a pattern speed of 37.5 km/s/kpc. Bovy et al. (2019) modelled the in-plane velocities (v_T, v_R) of giant stars as derived from *Gaia* DR2 and APOGEE data (Majewski et al. 2017; Leung & Bovy 2019) in the bar region ($2 < R/\text{kpc} < 5$). It also agrees with gas dynamics measurements by Weiner & Sellwood (1999) and Sormani et al. (2015). For the *MWPotential2014*, $\Omega_{\text{bar}} = 41 \pm 3$ km/s/kpc corresponds to $1.49 \pm 0.1\Omega_0$, for the Eilers et al. (2019) potential to $1.45 \pm 0.1\Omega_0$. Figure 12 overplots the *Gaia* actions for both potentials with the resonance lines for this pattern speed (including the uncertainty).

To distinguish it from the pattern speeds derived in this work, we refer to this *slightly faster slow bar* pattern speed $\Omega_{\text{bar}} = 41 \pm 3$ km/s/kpc as the S19B19 pattern speed, named after Sanders et al. (2019) and Bovy et al. (2019).

In our MW potential models for $\Omega_{\text{bar}} \sim 1.5\Omega_0$, it is the 1:4 resonance that falls right in between the ‘red/blue’ Hercules/Horn feature (see Figure 12). This agrees with the ‘Hercules/Horn = 1:4 resonance’ explanation by Hunt & Bovy (2018) (for a boxy bar

with $\alpha_{m=4} < 0$; see their fig. 5). A similar model was revisited in Hunt et al. (2019) (their model C) in action-angle-frequency space in different potential models, as well as in the $(R, v_T, \langle v_R \rangle)$ plane. They pointed out that this model’s OLR ridge lies in the wrong location in action space. And indeed, in our Figure 12, the inward-moving G1/orange Sirius ridge (not overplotted) around $L_z/L_{z,0} \sim 1.1$ could be the scattering ridge of the OLR for $\sim 1.5\Omega_0$, but no strong ‘red/blue’ feature exists close-by. In fact, it is close to (and for the Eilers et al. (2019) potential exactly on) the most prominent ‘blue/red’ transition in the data (i.e. the opposite way around).

The resonance locations of the S19B19 pattern speed with respect to the observed action ridges are therefore clearly distinct from those of the Hat and Sirius pattern speeds.

Two side notes on the lower and upper limits of the S19B19 pattern speed: Firstly, the upper limit ($\sim 1.6\Omega_0$ in the *MWPotential2014*) would make the S19B19 pattern speed agree with our Sirius pattern speed. A potential model with lower circular velocities would have the same effect. Secondly, for the lower limit of the S19B19 pattern speed ($\sim 1.4\Omega_0$ in the *MWPotential2014*), all four shown resonance lines align with transitions from inward- to outward-moving stripes (or vice versa). For the OLR it is the wrong way around, but it is still an interesting coincidence that the spacing of the sign-flips in v_R correspond to the spacings of these resonance lines.

To conclude, we tend to rule out the S19B19 pattern speed (for $\Omega_{\text{bar}} \sim 1.4 - 1.5\Omega_0$) because of the absence of the OLR’s characteristic ‘red/blue’ feature—unless we find an explanation, e.g. through obscuration by spiral structure (Hunt et al. 2019; Fujii et al. 2019), or modifications of V_\odot or $v_{\text{circ}}(R)$ (Monari et al. 2019a), or resonance sweeping by a decelerating bar (Chiba et al. 2019).

Further constraints are required. An obvious place to search is the space of phase-angles, which we investigate in a companion study, Trick et al. (in preparation).

7 CONCLUSION

We illustrated that the axisymmetric actions $\mathbf{J} = (J_R, L_z, J_z)$ estimated for the real MW stars in an axisymmetric MW potential model are still meaningful in the presence of—and even informative about—perturbations in the Galactic disc. In particular, we used the

axisymmetric resonance lines (ARLs), i.e. the line in (L_z, J_R) for a given (l, m) along which $m [\Omega_{\text{bar}} - \Omega_{\phi, \text{axi}}(\mathbf{J})] - l \Omega_{R, \text{axi}}(\mathbf{J}) = 0$ is satisfied, as a diagnostic tool for resonances of the Galactic bar.

We investigated the behaviour of individual stars in axisymmetric action space as response to an $m = 2$ bar model, by means of a test particle simulation that integrates orbits in an analytic barred MW potential. These numerical orbits confirm and illustrate what the field already knows about the characteristics of bar resonances:

- (i) All orbits in a bar-affected system *oscillate* in both L_z and J_R direction. Orbits trapped at resonances oscillate around the corresponding $l : m$ ARL. Closed periodic parent orbits swing only between peri- and apocenter. Orbits with the same Jacobi energy E_J librate in addition along lines of $\delta J_R / \delta L_z \sim l/m$, on which E_J is conserved.
- (ii) Resonances *scatter* stars (when considering their time-averaged oscillation midpoint with respect to their actions in the un-barred system) also along $\Delta J_R / \Delta L_z \sim l/m$. This— together with the disk population’s density gradients across the action plane—creates at the Outer Lindblad resonances $l = +1, m \in [1, 2]$ a high- J_R scattering ridge on the high- L_z side of the ARL, and an underdensity region on the low- L_z side. This is the action-analogue of the well-studied OLR signature in velocity space.
- (iii) It has long been known that the shape of the parent orbits flips its orientation with respect to the bar at the principal resonances, leading at the OLR to a sign-flip in radial velocity from outward- to inward-moving at the Solar azimuth. Action space visualizes this especially cleanly, with the flip occurring along the OLR ARL.

Building on these foundations, we have presented in this work two novel findings related to the ARLs and the OLR of the MW’s bar:

- (1) We showed that an $l : m$ ARL shifts its location in (L_z, J_R) with vertical action J_z , and that a resonant star has its oscillation midpoint (see (i) and (ii) above) close to the ARL that takes into account this star’s specific J_z . We demonstrated that this causes in the overall disk population at the resonances a gradient in $\langle J_z \rangle$ as a function of (L_z, J_R) which is especially strong at the OLR, with the underdensity region having a higher and the ridge having a lower $\langle J_z \rangle$. This proposes for the first time an additional mechanism that could contribute to the vertical patterns (i.e. in $\langle J_z \rangle$ and $\langle |v_z| \rangle$) observed in the *Gaia* DR2 data.
- (2) We proposed a straight-forward strategy to measure all bar pattern speed candidates Ω_{bar} directly and precisely from the *Gaia* DR2 RVS data. When colour-coding the action plane (L_z, J_R) by predominantly outward (‘red’) and predominantly inward motion (‘blue’), three pairs of ‘red/blue’ transitions are visible that have slopes similar to the OLR ARL. Varying the bar pattern speed Ω_{bar} and positioning the OLR ARL exactly on top of the ‘red/blue’ transitions—the expected signature of the OLR (see (iii) above)—gives precise measurements for Ω_{bar} candidates: $1.85\Omega_0$, $1.20\Omega_0$, and $1.63\Omega_0$, when assuming the $M_{\text{potential}2014}$ by Bovy (2015). When assuming the potential by Eilers et al. (2019), we measure $1.85\Omega_0$, $1.27\Omega_0$, and $1.70\Omega_0$. The first measurement is very close to the classic *fast* bar model in the literature with the OLR between the Hercules/horn moving groups. The second is slightly slower than the popular *slow* bar model from Galactic center measurements, with the Hat as the OLR scattering ridge. The last—which we call the *Sirius* pattern speed—revives an old proposition from

the literature and we show that it ‘red/blue’ moving features in action space with the OLR and with the 1:1 resonance line of the bar.

One of the above three pattern speeds has to be close to the real bar pattern speed, unless (a) our knowledge of the best-fit axisymmetric potential, in particular the rotation curve, of the MW is very wrong, (b) the OLR of the bar does not fall within the *Gaia* survey volume (which, however, is quite unlikely), or (c) spiral arms or other transient perturbations are so strong in the MW disc that the signature of the bar is washed out. We note that the disagreement between Galactic center measurements and our candidates points towards a missing piece in the puzzle of Ω_{bar} .

In any case, the signatures in axisymmetric actions space are highly informative about the true nature of perturbers in the Galactic disc.

DATA AVAILABILITY STATEMENT

This work has made use of data from *Gaia* DR2 (Gaia Collaboration et al. 2016, 2018a) available at <https://gea.esac.esa.int/archive>. For *Gaia* DR2’s radial velocity sample (Katz et al. 2019), stellar distances were taken from Schönrich et al. (2019) and are available at <https://zenodo.org/record/2557803>.

Action estimation and test particle simulations underlying this article were produced with the `galpy` code by Bovy (2015) which is publicly available at <http://github.com/jobovy/galpy>. The action data and simulations will be shared on reasonable request to the corresponding author.

ACKNOWLEDGEMENTS

W.H.T. thanks Jerry Sellwood, Benoit Famaey, Ortwin Gerhard, Jason Sanders, Christophe Pichon, as well as the White research group at MPA for helpful discussions, Irene Abril Cabezas and Adam Wheeler for providing useful comments on the draft, and the anonymous referee for many suggestions to improve this paper.

J.A.S.H. was supported by a Dunlap Fellowship at the Dunlap Institute for Astronomy & Astrophysics, funded through an endowment established by the Dunlap family and the University of Toronto. J.A.S.H. is now supported by a Flatiron Research Fellowship at the Flatiron institute, which is supported by the Simons Foundation.

J.T.M. acknowledges support from the ERC Consolidator Grant funding scheme (project ASTEROCHRONOMETRY, G.A. n. 772293).

This work has made use of data from the European Space Agency (ESA) mission *Gaia* (<https://www.cosmos.esa.int/gaia>), processed by the *Gaia* Data Processing and Analysis Consortium (DPAC, <https://www.cosmos.esa.int/web/gaia/dpac/consortium>). Funding for the DPAC has been provided by national institutions, in particular the institutions participating in the *Gaia* Multilateral Agreement.

This project was developed in part at the 2018 NYC *Gaia* Sprint, hosted by the Center for Computational Astrophysics of the Flatiron Institute in New York City.

This research was supported in part at KITP by the Heising-Simons Foundation and the National Science Foundation under Grant No. NSF PHY-1748958.

REFERENCES

- Antoja T., et al., 2014, *A&A*, **563**, A60
- Antoja T., et al., 2018, *Nature*, **561**, 360
- Arifyanto M. I., Fuchs B., 2006, *A&A*, **449**, 533
- Arnold V. I., 1978, *Mathematical methods of classical mechanics*
- Athanassoula E., 1992, *MNRAS*, **259**, 345
- Athanassoula E., Bienayme O., Martinet L., Pfenniger D., 1983, *A&A*, **127**, 349
- Athanassoula E., Machado R. E. G., Rodionov S. A., 2013, *MNRAS*, **429**, 1949
- Bensby T., Oey M. S., Feltzing S., Gustafsson B., 2007, *ApJ*, **655**, L89
- Binney J., 1981, *MNRAS*, **196**, 455
- Binney J., 2012, *MNRAS*, **426**, 1324
- Binney J., 2018, *MNRAS*, **474**, 2706
- Binney J., 2020a, *MNRAS*, **495**, 886
- Binney J., 2020b, *MNRAS*, **495**, 895
- Binney J., McMillan P., 2011, *MNRAS*, **413**, 1889
- Binney J., Spergel D., 1982, *ApJ*, **252**, 308
- Binney J., Tremaine S., 2008, *Galactic Dynamics: Second Edition*. Princeton University Press
- Bissantz N., Englmaier P., Gerhard O., 2003, *MNRAS*, **340**, 949
- Bovy J., 2015, *ApJS*, **216**, 29
- Bovy J., Rix H.-W., 2013, *ApJ*, **779**, 115
- Bovy J., Hogg D. W., Roweis S. T., 2009, *ApJ*, **700**, 1794
- Bovy J., Rix H.-W., Hogg D. W., Beers T. C., Lee Y. S., Zhang L., 2012, *ApJ*, **755**, 115
- Bovy J., Leung H. W., Hunt J. A. S., Mackereth J. T., García-Hernández D. A., Roman-Lopes A., 2019, *MNRAS*, **490**, 4740
- Buta R., Laurikainen E., Salo H., Block D. L., Knapen J. H., 2006, *AJ*, **132**, 1859
- Carrillo I., et al., 2019, *MNRAS*, **490**, 797
- Chakrabarty D., 2007, *A&A*, **467**, 145
- Chereul E., Creze M., Bienayme O., 1998, *A&A*, **340**, 384
- Chiba R., Friske J. K. S., Schönrich R., 2019, arXiv e-prints, p. arXiv:1912.04304
- Clarke J. P., Wegg C., Gerhard O., Smith L. C., Lucas P. W., Wylie S. M., 2019, *MNRAS*, **489**, 3519
- Contopoulos G., 1980, *A&A*, **81**, 198
- Contopoulos G., Grosbol P., 1989, *A&ARv*, **1**, 261
- D’Onghia E., L. Aguerri J. A., 2020, *ApJ*, **890**, 117
- De Simone R., Wu X., Tremaine S., 2004, *MNRAS*, **350**, 627
- Dehnen W., 1998, *AJ*, **115**, 2384
- Dehnen W., 2000, *AJ*, **119**, 800
- Eggen O. J., 1996, *AJ*, **112**, 1595
- Eilers A.-C., Hogg D. W., Rix H.-W., Ness M. K., 2019, *ApJ*, **871**, 120
- Englmaier P., Gerhard O., 1999, *MNRAS*, **304**, 512
- Famaey B., Jorissen A., Luri X., Mayor M., Udry S., Dejonghe H., Turon C., 2005, *A&A*, **430**, 165
- Famaey B., Pont F., Luri X., Udry S., Mayor M., Jorissen A., 2007, *A&A*, **461**, 957
- Famaey B., Siebert A., Jorissen A., 2008, *A&A*, **483**, 453
- Fouvry J.-B., Pichon C., 2015, *MNRAS*, **449**, 1982
- Fouvry J.-B., Pichon C., Prunet S., 2015a, *MNRAS*, **449**, 1967
- Fouvry J. B., Pichon C., Chavanis P. H., 2015b, *A&A*, **581**, A139
- Fouvry J. B., Pichon C., Magorrian J., Chavanis P. H., 2015c, *A&A*, **584**, A129
- Fouvry J.-B., Binney J., Pichon C., 2015d, *ApJ*, **806**, 117
- Fragkoudi F., et al., 2019, *MNRAS*, **488**, 3324
- Fragkoudi F., et al., 2020, *MNRAS*, **494**, 5936
- Friske J. K. S., Schönrich R., 2019, *MNRAS*, **490**, 5414
- Fujii M. S., Bédorf J., Baba J., Portegies Zwart S., 2019, *MNRAS*, **482**, 1983
- Fux R., 1999, *A&A*, **345**, 787
- Fux R., 2001, *A&A*, **373**, 511
- Gaia Collaboration et al., 2016, *A&A*, **595**, A1
- Gaia Collaboration et al., 2018a, *A&A*, **616**, A1
- Gaia Collaboration et al., 2018b, *A&A*, **616**, A11
- Gómez F. A., Helmi A., Brown A. G. A., Li Y.-S., 2010, *MNRAS*, **408**, 935
- Gómez F. A., Minchev I., Villalobos Á., O’Shea B. W., Williams M. E. K., 2012, *MNRAS*, **419**, 2163
- Halle A., Di Matteo P., Haywood M., Combes F., 2018, *A&A*, **616**, A86
- Helmi A., White S. D. M., de Zeeuw P. T., Zhao H., 1999, *Nature*, **402**, 53
- Helmi A., Veljanoski J., Breddels M. A., Tian H., Sales L. V., 2017, *A&A*, **598**, A58
- Hinkel A., Gardner S., Yanny B., 2020, *ApJ*, **899**, L14
- Hunt J. A. S., Bovy J., 2018, *MNRAS*, **477**, 3945
- Hunt J. A. S., Hong J., Bovy J., Kawata D., Grand R. J. J., 2018, *MNRAS*, **481**, 3794
- Hunt J. A. S., Bub M. W., Bovy J., Mackereth J. T., Trick W. H., Kawata D., 2019, *MNRAS*, **490**, 1026
- Kaasalainen M., 1994, *MNRAS*, **268**, 1041
- Kalnajs A. J., 1971, *ApJ*, **166**, 275
- Kalnajs A. J., 1991, in Sundelius B., ed., *Dynamics of Disc Galaxies*. p. 323
- Katz D., et al., 2019, *A&A*, **622**, A205
- Kawata D., Baba J., Ciucă I., Cropper M., Grand R. J. J., Hunt J. A. S., Seabroke G., 2018, *MNRAS*, **479**, L108
- Khanna S., et al., 2019, *MNRAS*, **489**, 4962
- Khoperskov S., Gerhard O., Di Matteo P., Haywood M., Katz D., Khrapov S., Khoperskov A., Arnaboldi M., 2020, *A&A*, **634**, L8
- Klement R., Fuchs B., Rix H. W., 2008, *ApJ*, **685**, 261
- Koppelman H., Helmi A., Veljanoski J., 2018, *ApJ*, **860**, L11
- Kunder A., et al., 2012, *AJ*, **143**, 57
- Laporte C. F. P., Minchev I., Johnston K. V., Gómez F. A., 2019, *MNRAS*, **485**, 3134
- Laskar J., 1993, *Celestial Mechanics and Dynamical Astronomy*, **56**, 191
- Leung H. W., Bovy J., 2019, *MNRAS*, **489**, 2079
- Li Z., Gerhard O., Shen J., Portail M., Wegg C., 2016, *ApJ*, **824**, 13
- Long R. J., Mao S., Shen J., Wang Y., 2013, *MNRAS*, **428**, 3478
- Lynden-Bell D., 1979, *MNRAS*, **187**, 101
- Lynden-Bell D., Kalnajs A. J., 1972, *MNRAS*, **157**, 1
- Majewski S. R., et al., 2017, *AJ*, **154**, 94
- Martinet L., Magnenat P., Verhulst F., 1981, *Celestial Mechanics*, **25**, 93
- Masset F., Tagger M., 1997, *A&A*, **318**, 747
- McMillan P. J., 2011a, *MNRAS*, **414**, 2446
- McMillan P. J., 2011b, *MNRAS*, **418**, 1565
- Minchev I., 2016, *Astronomische Nachrichten*, **337**, 703
- Minchev I., Nordhaus J., Quillen A. C., 2007, *ApJ*, **664**, L31
- Minchev I., Quillen A. C., Williams M., Freeman K. C., Nordhaus J., Siebert A., Bienaymé O., 2009, *MNRAS*, **396**, L56
- Minchev I., Boily C., Siebert A., Bienaymé O., 2010, *MNRAS*, **407**, 2122
- Monari G., Famaey B., Siebert A., 2016a, *MNRAS*, **457**, 2569
- Monari G., Famaey B., Siebert A., Grand R. J. J., Kawata D., Boily C., 2016b, *MNRAS*, **461**, 3835
- Monari G., Famaey B., Siebert A., Duchateau A., Lorscheider T., Bienaymé O., 2017a, *MNRAS*, **465**, 1443
- Monari G., Kawata D., Hunt J. A. S., Famaey B., 2017b, *MNRAS*, **466**, L113
- Monari G., Famaey B., Fouvry J.-B., Binney J., 2017c, *MNRAS*, **471**, 4314
- Monari G., Famaey B., Siebert A., Wegg C., Gerhard O., 2019a, *A&A*, **626**, A41
- Monari G., Famaey B., Siebert A., Bienaymé O., Ibata R., Wegg C., Gerhard O., 2019b, *A&A*, **632**, A107
- Mühlbauer G., Dehnen W., 2003, *A&A*, **401**, 975
- Myeong G. C., Evans N. W., Belokurov V., Sanders J. L., Koposov S. E., 2018, *MNRAS*, **478**, 5449
- Nordström B., et al., 2004, *A&A*, **418**, 989
- Pérez-Villegas A., Portail M., Wegg C., Gerhard O., 2017, *ApJ*, **840**, L2
- Portail M., Gerhard O., Wegg C., Ness M., 2017, *MNRAS*, **465**, 1621
- Quillen A. C., 2003, *AJ*, **125**, 785
- Quillen A. C., Minchev I., 2005, *AJ*, **130**, 576
- Quillen A. C., et al., 2018, *MNRAS*, **480**, 3132
- Rauch K. P., Tremaine S., 1996, *New Astron.*, **1**, 149
- Rix H.-W., Bovy J., 2013, *A&ARv*, **21**, 61
- Rodriguez-Fernandez N. J., Combes F., 2008, *A&A*, **489**, 115
- Sanders J. L., Binney J., 2016, *MNRAS*, **457**, 2107

- Sanders R. H., Huntley J. M., 1976, *ApJ*, 209, 53
 Sanders J. L., Smith L., Evans N. W., 2019, *MNRAS*, 488, 4552
 Schönrich R., Dehnen W., 2018, *MNRAS*, 478, 3809
 Schönrich R., Binney J., Dehnen W., 2010, *MNRAS*, 403, 1829
 Schönrich R., McMillan P., Eyer L., 2019, *MNRAS*, 487, 3568
 Sellwood J. A., 2010, *MNRAS*, 409, 145
 Sellwood J. A., 2012, *ApJ*, 751, 44
 Sellwood J. A., Binney J. J., 2002, *MNRAS*, 336, 785
 Sellwood J. A., Lin D. N. C., 1989, *MNRAS*, 240, 991
 Sellwood J. A., Wilkinson A., 1993, *Reports on Progress in Physics*, 56, 173
 Sellwood J. A., Trick W. H., Carlberg R. G., Coronado J., Rix H.-W., 2019, *MNRAS*, 484, 3154
 Smith L. C., et al., 2018, *MNRAS*, 474, 1826
 Sormani M. C., Binney J., Magorrian J., 2015, *MNRAS*, 454, 1818
 Struck C., 2015, *MNRAS*, 450, 2217
 Toomre A., 1981, in Fall S. M., Lynden-Bell D., eds, *Structure and Evolution of Normal Galaxies*. pp 111–136
 Tremaine S., Weinberg M. D., 1984, *ApJ*, 282, L5
 Trick W. H., Bovy J., Rix H.-W., 2016, *ApJ*, 830, 97
 Trick W. H., Bovy J., D’Onghia E., Rix H.-W., 2017, *ApJ*, 839, 61
 Trick W. H., Coronado J., Rix H.-W., 2019, *MNRAS*, 484, 3291
 Wegg C., Gerhard O., 2013, *MNRAS*, 435, 1874
 Weinberg M. D., 1994, *ApJ*, 420, 597
 Weinberg M. D., 2001, *MNRAS*, 328, 311
 Weiner B. J., Sellwood J. A., 1999, *ApJ*, 524, 112

APPENDIX A: TIME EVOLUTION AND AZIMUTHAL DEPENDENCE OF THE OLR SIGNATURE

Figure A1 shows for the Fiducial simulation the time evolution of the OLR signature from Section 5.1: the underdensity-region/overdensity-ridge signature around the OLR ARL in the upper panels, and the associated outward/inward feature at the Solar azimuth in the lower panels. We show both as a function of Galactic azimuth ϕ and L_z , which can be considered as the average radius of the star’s orbit. The first few Gyr of orbit integration in the barred potential are marked by the (unrealistic) transition phase away from axisymmetry (first column). The characteristic, steady-state OLR signature due to the orbit pattern with its azimuthal $m = 2$ symmetry with respect to the bar has been established.

APPENDIX B: OSCILLATION AMPLITUDE ACROSS THE ACTION PLANE

Orbits oscillate in the space of axisymmetric actions due to the rotating bar potential (Section 4.5) around the midpoints \mathbf{J}_{mean} illustrated in Figure 5. Figure B1 shows for the Fiducial simulation the *average oscillation amplitudes*, i.e. δL_z and δJ_R , which were calculated from the numerically integrated orbits as

$$\delta J_R = \frac{1}{2} (\max [J_R(t)] - \min [(J_R(t))]) \quad (\text{B1})$$

and equivalently for δL_z . We show these in the $(L_{z,\text{mean}}, J_{R,\text{mean}})$ and the $(L_{z,\text{mean}}, \phi)$ planes, respectively, where ϕ is the Galactocentric azimuth at $t = 25T_{\text{bar}}$. Figure B1(a) demonstrates that stars that are on $x_1(1)$ orbits oscillate strongly in J_R (and L_z) around the OLR ARL (c.f. Figure 6, Section 4.6, and Fragkoudi et al. (2019)). Figure B1(b) shows the strong oscillation δL_z at CR. This mixes resonant with non-resonant stars and washes out resonance features, which are therefore less prominent than at the OLR.

APPENDIX C: DETAILS OF THE TEST PARTICLE SIMULATION

C1 The axisymmetric stellar disc model

The test particle simulation is set up in the analytic axisymmetric MWPotential2014 by Bovy (2015). We mimic an axisymmetric, exponential stellar disc by sampling the action-based quasi-isothermal DF by Binney & McMillan (2011). This qDF requires the potential as input and ensures that the collisionless Boltzmann equation is satisfied. The resulting stellar distribution is phase-mixed by construction. We use the same qdf parameters as for the mock data in T19, which roughly reproduce the velocity dispersion of *Gaia* DR2 in the Solar neighbourhood, $\sigma_{z,0}^{\text{qdf}} = 20$ km/s and $\sigma_{R,0}^{\text{qdf}} = 37$ km/s. The vertical velocity dispersion is exponentially decreasing with radius with a scale length of $h_{\sigma,z}^{\text{qdf}} = 7$ kpc (Bovy et al. 2012).

We restrict the sampling of the mock data to the large annulus around the galactic center illustrated in Figure C1(a): $R \in [3, 17]$ kpc, $|z| < 1$ kpc, $\phi \in [-\pi, \pi]$ rad. The exact mock data generation procedure is described in appendix A of Trick et al. (2016).

Figure C1(b) shows the distribution of the axisymmetric mock data in the action plane (L_z, J_R) . The sharp unrealistic radial edges of the annulus cause phase artifacts in the distribution. We therefore show the action data only for the range $L_z \in [0.5, 1.8]L_{z,0}$ within which the mock data are fully phase-mixed, as required. (L_z, J_R) are in this setup the “real” actions of the orbits, i.e. they are true integrals of motion and stay constant along the orbit if integrated in the axisymmetric potential. Their distribution is smooth and nicely illustrates the realistic property of the qdf that stars in the inner galaxy (at smaller L_z) are more numerous and on “hotter” orbits (i.e. have larger J_R on average).

C2 Orbit integration in the barred galaxy potential

In a second step, we in the test particle simulation the quadrupole bar by Dehnen (2000), generalized to 3D by Monari et al. (2016b), implemented in galpy. Its strength $\alpha_{m=2} = 0.01$ is the ratio of the maximum radial force at R_0 due to the ($m = 2$) bar potential alone to the axisymmetric background potential. This bar strength is similar to those used by, e.g., Monari et al. (2017a) and Hunt et al. (2019). In the surface density of the stellar component of the potential, the bar imposes outside of $R \sim 1$ kpc a maximum perturbation of $A_2 = 0.26$ (following the definition of A_2 by Athanassoula et al. 2013). The parameters for the Fiducial bar model are summarized in Table 1. The total mass of the bar is zero. When imposing it onto the MWPotential2014 it can be considered as a redistribution of the matter (see Figure C1(c)). Averaged over ϕ , the circular velocity curve is the same as for the purely axisymmetric galaxy model.

The bar strength is instantaneously switched on from zero to its full value at time $t = 0$. Similar studies usually grow the bar adiabatically from zero to its full strength to avoid a shock to the system (e.g. Mühlbauer & Dehnen 2003; Minchev et al. 2010; Hunt et al. 2019). We have run additional test simulations that grow the bar over $N = 15$ bar periods. The qualitative bar signatures were very similar. The reasons are: (i) The particles are massless. The disc distribution is therefore not modified by self-gravity and the wake that the bar induces. A star’s orbit depends only on its current (\mathbf{x}, \mathbf{v}) and the analytic potential model without knowledge of its past orbital evolution. No shocks are therefore induced. (ii) The qdf we used to set-up the system generates a stellar population in steady-

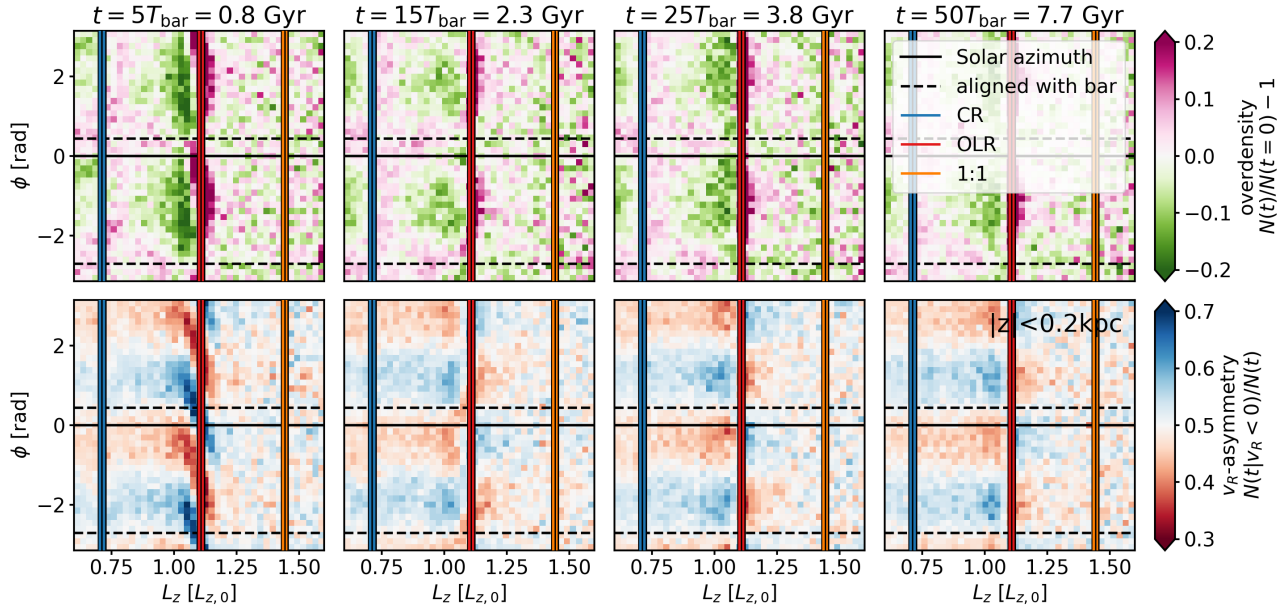


Figure A1. Time evolution of the OLR signature in the fiducial bar simulation as a function of Galactic azimuth ϕ . The x-axis shows L_z , i.e. the guiding center radius, and the vertical lines the location of the OLR (red), CR (blue) and 1:1 (orange) ARLs evaluated at $J_R \in [0, 0.01]L_{z,0}$ and $J_z = 0$. Around the OLR line, we see the underdensity region and the overdensity ridge and the characteristic asymmetry between inward- and outward moving stars. The first column captures the transition from the axisymmetric to the bar affected state in the simulation. After a few Gyr of orbit integration, the OLR pattern remains stable with respect to the bar.

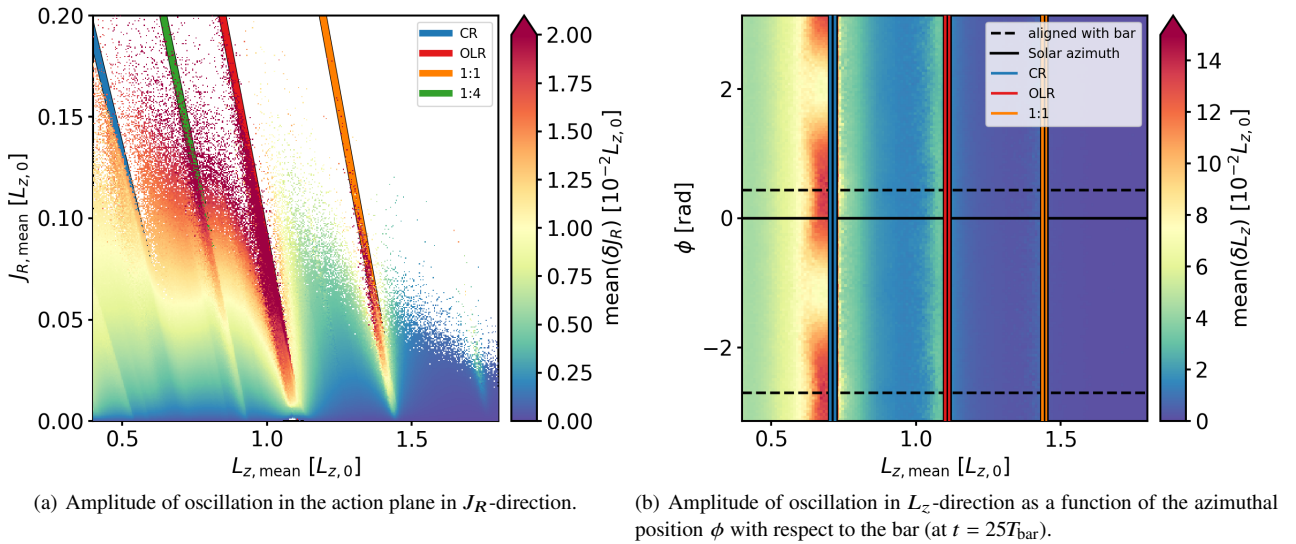


Figure B1. Oscillation amplitudes of bar affected orbits in J_R (left panel) and L_z (right panel) direction as a function of the oscillation midpoints J_{mean} .

state. As long as the bar is weak, the system remains in almost the same steady-state.

We integrate particle orbits in the barred potential using the RK4 method provided by `galpy`. At integration times of $t = 0$ and $t = n \times T_{\text{bar}} \equiv 2\pi n / \Omega_{\text{bar}}$, $n \in \mathbb{N}$, the bar is orientated at an angle of 25 degrees with respect to the $x = 0$ line (see Figure C1(c) and (d)), similar to the angle between the Galactic bar and the line-of-sight line between the Galactic center and the Sun (Bovy et al. 2019). The lower panels in Figure C1 show the distribution after 25 bar periods, which corresponds to 3.8 Gyr. This time was chosen to

be well past the initial transition from the axisymmetric to the bar-affected system (see Figure A1 and fig. 2 in Mühlbauer & Dehnen 2003). We applied an additional cut of $|z| < 500$ pc to reduce artifacts in the vertical phase and action due to the vertical cut in the initial conditions.

The bar-affected action distribution of all particles in Figure C1(e) is overplotted by the resonance ARLs. As our simulation is restricted to the action distribution outside of $L_z = 0.4L_{z,0}$, we cannot pick up any resonant signatures inside the CR.

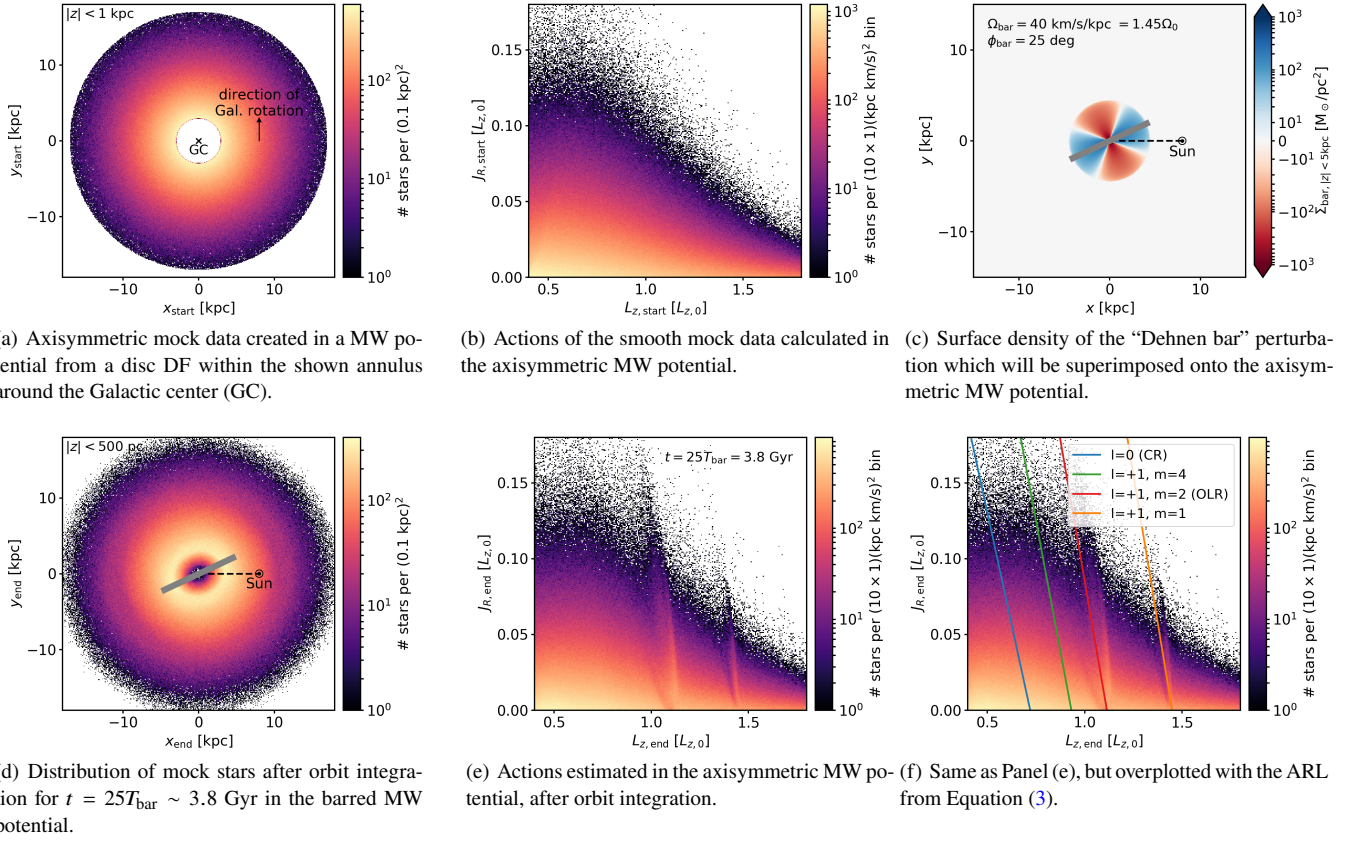


Figure C1. Illustration of the mock data simulation with test particles in a barred MW potential for the Fiducial bar model in Table 1. Panels (a)-(b) show the axisymmetric mock data before orbit integration; Panels (d)-(f) the distribution after integration in the barred potential (Panel (c)). Ridges have developed next to the OLR and 1:1 ARLs.

This paper has been typeset from a $\text{\TeX}/\text{\LaTeX}$ file prepared by the author.